Reliable ADMM-Based Signal Detection for OTFS-DCSK Under High-Mobility Scenarios

Zhaofeng Liu, Zhi-Yong Wang, Hing Cheung So, Fellow, IEEE, Zuwei Chen, Lin Zhang, Senior Member, IEEE, and Tse-Tin Chan, Member, IEEE

Abstract—High-mobility scenarios have increasingly attracted attention due to their relevance in modern wireless communication systems, where doubly selective fading (DSF) significantly degrades transmission reliability. To address this issue, we propose a transceiver that combines orthogonal time frequency space (OTFS) modulation with differential chaos shift keying (DCSK) to provide robustness against DSF. In this design, mapping symbols onto the OTFS delay-Doppler (DD) grid exploits DD diversity, delivering high reliability under DSF and achieving markedly lower bit error rate than conventional schemes. To fully realize these advantages, this paper devises an alternating direction method of multipliers (ADMM)-based signal detection method tailored specifically for OTFS-DCSK. Our solution employs the least squares QR (LSQR) algorithm to leverage channel sparsity, along with truncated singular value decomposition (SVD) to exploit the rank-1 structure of the transmitted symbols, achieving effective noise reduction. Both LSQR and SVD exhibit acceptable complexity, resulting in a computationally efficient detector. Simulation results verify that the developed ADMM algorithm significantly improves reliability, yielding lower normalized mean squared error and bit error rate compared to existing approaches under DSF channels.

Index Terms—Orthogonal time frequency space; differential chaos shift keying; alternating direction method of multipliers; high-mobility scenarios; doubly selective fading; reliability.

I. INTRODUCTION

Wireless communication systems are particularly susceptible to attacks by malicious users due to their open access and broadcasting nature. Chaotic communication has emerged as a technique to enhance the security of wireless transmissions by leveraging the properties of chaotic sequences, such as extreme sensitivity to initial conditions and inherent randomness, which make the signals unpredictable and difficult to intercept [1], [2]. These characteristics make chaotic communication techniques extensively applicable in data transmission across various domains, including ultra-wide-band (UWB) [2], [3], power line communication (PLC) [4], and vehicle-to-vehicle

Manuscript received 2 April, 2025, revised 18 July, 2025, accepted 1 September, 2025. This work was supported in part by the Research Matching Grant Scheme from the Research Grants Council of Hong Kong. (Corresponding author: Zhi-Yong Wang.)

Zhaofeng Liu, Zhi-Yong Wang, Hing Cheung So, and Zuwei Chen are with the Department of Electrical Engineering, City University of Hong Kong, Hong Kong SAR, China (e-mail: zhaofeliu3-c@my.cityu.edu.hk; z.y.wang@my.cityu.edu.hk; hcso@ee.cityu.edu.hk; zuweichen2-c@my.cityu.edu.hk).

Lin Zhang is with the School of Cyber Science and Technology, Sun Yatsen University, Shenzhen, China (e-mail: isszl@mail.sysu.edu.cn).

Tse-Tin Chan is with the Department of Mathematics and Information Technology, The Education University of Hong Kong, Hong Kong SAR, China (e-mail: tsetinchan@eduhk.hk).

(V2V) communications [5]. Chaotic modulation, which exploits chaotic sequences to modulate information bits, can be divided into coherent and non-coherent types. The main distinction lies in the necessity for chaotic sequence regeneration at the receiver in the former, whereas the latter has no such requirement, making it simpler and more prevalently utilized [6], [7].

Among various non-coherent chaotic modulation techniques, differential chaos shift keying (DCSK) has garnered significant interest [7]. DCSK involves transmitting a reference chaotic sequence followed by an information-bearing chaotic sequence, which is created by modulating the reference sequence with binary phase shift keying (BPSK) symbols. This approach obviates the need for chaotic waveform regeneration at the receiver, thereby eliminating the requirement for chaos synchronization and substantially reducing system complexity. DCSK has proven effective in delivering satisfactory bit error rate (BER) in diverse environments such as UWB, PLC, and V2V communications, ensuring reliable data transmission [2]. However, the transmission efficiency of DCSK is relatively low because it necessitates sending two sequences in separate time slots for a single symbol, as well as complex delay line circuits [8].

To improve the transmission efficiency, several M-ary modulation schemes using Hilbert transform [9]–[11], Walsh code [12], and index modulation [13] have been introduced. Nevertheless, they do not solve the issue with delay lines. A viable alternative to eliminate delay lines is to distribute different sequences across various subcarriers rather than different time slots, a strategy central to multi-carrier (MC) transmission. In MC-based DCSK systems, a single reference sequence can demodulate multiple information-bearing sequences, significantly boosting transmission efficiency compared to traditional DCSK systems [14]. Additionally, to reduce MC-DCSK complexity, orthogonal frequency division multiplexing (OFDM) is employed via fast Fourier transform (FFT) [15], assuming that the number of subcarriers is power of 2.

While OFDM offers a flexible framework for mitigating multipath fading in DCSK systems [16], it is notably sensitive to Doppler shifts, or time-selective fading, which arises from the relative motion between the transmitter and receiver. This is particularly problematic in high-mobility scenarios [17] such as V2V communications [5], [18]. Doppler shifts can induce inter-carrier interference (ICI) [19], adversely affecting the performance of OFDM-based DCSK systems. To mitigate carrier frequency offsets caused by Doppler shifts, [20] presents a pre-coding OFDM-DCSK system, but it leads to a

1

duplication of information symbols, hence reducing spectral efficiency. Moreover, doubly selective fading (DSF), which combines the effects of Doppler shifts and multipath fading, can severely compromise the reliability of OFDM-DCSK systems. A novel approach in [21] employs singular value decomposition (SVD)-based pre-coding and permutation to address DSF in OFDM-DCSK systems. However, this solution necessitates that both the transmitter and receiver possess channel state information (CSI), which can increase the overall system complexity.

By contrast, orthogonal time frequency space (OTFS) modulation offers advantages over OFDM in dealing with highmobility [22]. By utilizing the inverse symplectic finite Fourier transform (ISFFT) and symplectic finite Fourier transform (SFFT), OTFS transmits the symbols in the delay-Doppler (DD) domain rather than the time-frequency (TF) domain. Owing to the signal representation in the DD domain, OTFS is inherently more robust to Doppler shifts, making it a suitable choice for high-mobility scenarios [23]. Moreover, OTFS efficiently copes with multipath propagation by capturing the channel's delay spread in the DD domain, leading to a reduction in inter-symbol interference (ISI) and improved performance [24]. In fact, OTFS has emerged as a promising waveform candidate for next-generation communications [25], with recent research covering performance benchmarking against OFDM [26], advanced signal processing [27], multiple-input multiple-output enhancements [28], [29], spatial modulation integration [30], [31], and practical implementation aspects [32].

The DD representation of the OTFS signal exhibits a blockbased structure, akin to the OFDM-DCSK signal. In the OTFS scheme, information symbols are mapped onto a twodimensional DD grid, whereas OFDM-DCSK systems also employ a similar block-based structure, where data are transmitted over multiple orthogonal subcarriers, each modulated with a chaotic sequence. This similarity naturally motivates the application of OTFS modulation to DCSK-based systems to effectively combat DSF. OTFS achieves markedly lower BER than OFDM in DSF channels by exploiting full DD diversity [33]. Furthermore, [34] claims that OTFS can achieve high reliability over DSF channels due to the domain adaptivity. By integrating OTFS with DCSK, the resultant system leverages OTFS's robustness in dynamic channels to significantly improve reliability. In addition, due to OTFS's block-based structure, only one cyclic prefix (CP) is required to mitigate ISI [24]. In comparison, OFDM-DCSK modulation requires multiple CPs, thus making OTFS-based systems exhibit increased spectral efficiency in comparison to their OFDM-based counterparts.

Although OTFS effectively combats DSF, signal detection at the receiver presents significant challenges. The channel response matrix of the OTFS transmission model may have large dimensions, which complicates the minimum mean square error (MMSE) based detection in terms of computational requirements. Markov chain Monte Carlo (MCMC) sampling, utilized in OTFS signal detection [35], also faces substantial complexity issue because it fails to leverage the sparsity of the OTFS channel response matrix. Various methods have been

suggested to manage OTFS signal detection complexity by exploiting this sparsity, such as message passing (MP) [24] and maximal ratio combining (MRC) [36]. Nevertheless, these schemes require a finite-length codebook for modulated digital symbols, which is incompatible with the continuous nature of chaotic symbols used in DCSK systems. Few studies focus on using OTFS to enhance the reliability of DCSK systems over DSF channels. [37] designs an OTFS-DCSK system to counteract Doppler shifts. However, this approach requires each information-bearing sequence to have a unique reference sequence, resulting in a large symbol matrix and lower transmission efficiency. While [38] addresses the efficiency issue, its SVD-based symbol detector does not take into account the sparsity of the channel response matrix, potentially limiting its performance over DSF channels.

Since the OTFS-based DCSK system modulates multiple information-bearing sequences with one reference sequence, the resultant signal represented in matrix form has rank-1. Fully exploiting this property significantly reduces noise and increases system reliability [39]-[41]. This paper proposes integrating OTFS with DCSK to boost reliability over DSF channels and ensure high robustness against multipath fading and Doppler shifts. The system adopts OTFS modulation using ISFFT at the transmitter and SFFT at the receiver. To decode signals from the received OTFS-DCSK transmission frame, we introduce an alternating direction method of multipliers (ADMM)-based signal detector where the least squares QR (LSQR) [42] is adopted to handle the OTFS channel response matrix of large size, leveraging its sparsity to reduce computational complexity. Furthermore, SVD is utilized to reduce noise in the received signal. LSQR and SVD are alternately performed until the stopping criterion is met. Adopting this ADMM-based detector, the system delivers outstanding reliability performance over DSF channels.

Our novelty and technical contributions are listed as follows:

- We design an OTFS-DCSK transceiver structure to enhance system reliability over DSF channels.
- 2) We propose an ADMM-based signal detector that leverages the sparsity of the channel response matrix and the rank-1 property of the transmitted noise-free data matrix.
- 3) The convergence of the OTFS-DCSK signal detection algorithm is studied. The BER is derived for DSF channel and the diversity gain is also analyzed. Additionally, we study the spectral efficiency and complexity, with comparison with the competing methods.
- 4) We conduct extensive simulation study for our proposed scheme. According to the numerical results, our algorithm exhibits faster convergence speed and attains lower normalized mean squared error (NMSE) and BER compared to existing methods over DSF channels.

The organization of the paper is as follows: Section II introduces the OTFS-DCSK transceiver structure, featuring signal detection. The corresponding ADMM-based algorithm is detailed in Section III. Section IV analyzes convergence, BER, diversity gain, spectral efficiency, and complexity. Section V presents simulation results to assess the system performance by comparing with competing approaches. Section VI

concludes the paper.

II. PROPOSED OTFS-DCSK TRANSCEIVER

In this section, we present the structure of our OTFS-DCSK transceiver.

A. Transmitter Design

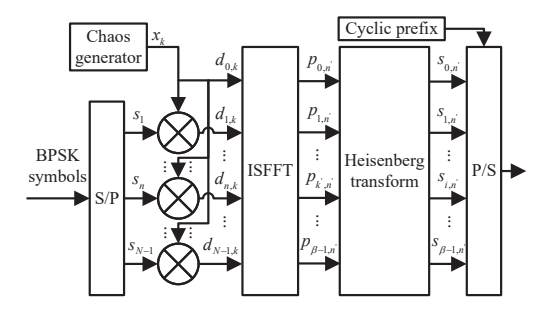


Fig. 1. Block diagram of OTFS-DCSK transmitter.

Fig. 1 depicts the block diagram of the OTFS-DCSK transmitter. The main modification compared to OFDM-DCSK [15] is the addition of ISFFT before the Heisenberg transform, where the Heisenberg transform is implemented by inverse fast Fourier transform (IFFT). The chaos generator initially produces chaotic sequences using the second-order Chebyshev polynomial function (CPF). This method is characterized by its high sensitivity to initial conditions and good pseudorandom properties, making it suitable for generating chaotic sequences in communication systems. The CPF is:

$$x_{k+1} = 1 - 2x_k^2, \quad x_k \in (-1, 0) \cup (0, 1)$$
 (1)

where x_k represents the kth chaotic chip and should strictly remain within (-1,0) or (0,1), $0 \le k \le \beta - 1$ and β denotes the sequence length. Chaotic modulation involves multiplying this sequence by the BPSK data symbols, which carry information bits after the serial-to-parallel (S/P) conversion. It is worth mentioning that as an extension, high-order modulation schemes can be adopted in the input data stream. For the kth chip on the nth subcarrier, the expression is $d_{n,k} = s_n x_k$. Here, indices $1 \le n \le N-1$ correspond to information-bearing sequences, while n=0 signifies the reference sequence with $d_{0,k} = x_k$ and N denotes the number of chaos sequences. $\{d_{n,k}\}$ for $0 \le k \le \beta-1$, $0 \le n \le N-1$ forms an OTFS-DCSK symbol in the DD domain, which can be represented as matrix form, denoted by D:

$$\boldsymbol{D} = \boldsymbol{c}_r \boldsymbol{s}^T \in \mathbb{R}^{\beta \times N} \tag{2}$$

where \mathbb{R} denotes the real number set, $(\cdot)^T$ denotes the transpose, $\boldsymbol{c}_r = [c_0, c_1, \dots, c_{\beta-1}]^T \in \mathbb{R}^{\beta}$ is the reference chaos sequence, and $\boldsymbol{s} = [1, s_1, \dots, s_{N-1}]^T \in \mathbb{R}^N$ is the BPSK symbol vector. Apparently, \boldsymbol{D} is a rank-1 matrix, and this property can be utilized for noise reduction. Following chaotic modulation, ISFFT is performed to map $\{d_{n,k}\}$ in the DD domain to $\{p_{k',n'}\}$ in the TF domain. The ISFFT process is realized as [23]:

$$p_{k',n'} = \frac{1}{\sqrt{N\beta}} \sum_{n=0}^{N-1} \sum_{k=0}^{\beta-1} d_{n,k} e^{j2\pi \left(\frac{n'n}{N} - \frac{k'k}{\beta}\right)}$$
(3)

where n, k, n', and k' denote the Doppler, delay, time, and frequency indices, respectively, $0 \le n' \le N-1$, $0 \le k' \le \beta-1$. Subsequently, the Heisenberg transform is employed to convert the TF signal into the time domain. The Heisenberg transform generalizes the inverse discrete Fourier transform (IDFT), making the IDFT its special case under the assumption of rectangular pulse shape. When the number of sample points is a power of 2, the IDFT can be efficiently computed using the IFFT. The IFFT applied to $p_{k',n'}$ for different values of k' is given by:

$$s_{i,n'} = \frac{1}{\sqrt{\beta}} \sum_{k'=0}^{\beta-1} p_{k',n'} e^{\frac{j2\pi k'i}{\beta}}$$
 (4)

where $\{s_{i,n'}\}$ for $0 \le i \le \beta - 1$, $0 \le n' \le N - 1$ forms an OTFS-DCSK symbol in the TF domain.

Chaotic spreading disperses signal power over a wide frequency range, driving the information-bearing symbols below the average noise floor. The resulting wideband spectrum substantially improves resilience to narrowband interference and jamming [43], allowing the system to reject both intentional and unintentional interference, and maintain reliable communication in hostile environments. By integrating OTFS with DCSK, the proposed OTFS-DCSK scheme retains OTFS robustness in DSF channels while offering spread-spectrum interference suppression. Compared with conventional OTFS which relies solely on DD mapping, OTFS-DCSK provides stronger immunity to interference and jamming, enhancing overall performance in DSF conditions.

At the end of the transmitter, the parallel data streams are converted to a serial format by the parallel-to-serial (P/S) converter. In the serial stream, $\{s_{i,n'}\}$ with smaller n' is transmitted first. For the same n', the values of i are compared, and the symbols with smaller i are transmitted first. After the P/S conversion, a CP is added to mitigate ICI and ISI. For one $\beta \times N$ OTFS-DCSK symbol block, only one CP is required, while for one $N \times \beta$ OFDM-DCSK symbol block [15], β CPs are needed. This indicates higher spectral efficiency of OTFS-DCSK compared to OFDM-DCSK, as the length of a single CP in both systems is identical. After appending CP, the symbols are transmitted through the wireless channels. This work assumes that the channels remain time-invariant over one OTFS-DCSK TF symbol and its CP.

B. Receiver Design

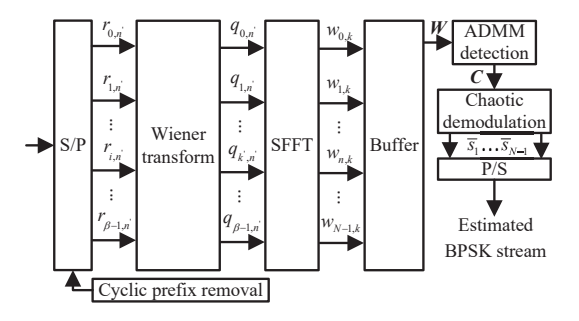


Fig. 2. Block diagram of OTFS-DCSK receiver.

The receiver structure incorporating the ADMM-based signal detection is illustrated in Fig. 2. The receiver first removes

the CP from the received data and performs S/P conversion. $r_{i,n'}$ denotes the symbol in the ith data stream and the n'th time slot. The Wigner transform applied to $r_{i,n'}$ for different values of i generates the TF domain signal. Under the assumption of rectangular pulse shape, the discrete Fourier transform (DFT) can be viewed as a special case of the Wigner transform. When the number of sample points is a power of 2, the DFT can be efficiently computed using the FFT as:

$$q_{k',n'} = \frac{1}{\sqrt{\beta}} \sum_{i=0}^{\beta-1} r_{i,n'} e^{\frac{-j2\pi ik'}{\beta}}.$$
 (5)

After the FFT, SFFT is applied, given by [23]:

$$w_{n,k} = \frac{1}{\sqrt{N\beta}} \sum_{n'=0}^{N-1} \sum_{k'=0}^{\beta-1} q_{k',n'} e^{-j2\pi \left(\frac{n'n}{N} - \frac{k'k}{\beta}\right)}$$
(6)

where $w_{n,k}$ is the (k,n) entry of $\boldsymbol{W} \in \mathbb{C}^{\beta \times N}$ with \mathbb{C} being the complex number set.

After the SFFT, the ADMM algorithm is employed for signal detection. Before depicting the detection process, we introduce the channel model first, and present the OTFS modulation and demodulation processes in matrix forms. We assume that a control channel is used to obtain CSI at the receiver and the channel is time-invariant during one OTFS-DCSK symbol. Denoting $s_{i,n'}$ and $r_{i,n'}$ as the (i,n') entry of $\mathbf{S} \in \mathbb{C}^{\beta \times N}$ and $\mathbf{R} \in \mathbb{C}^{\beta \times N}$ respectively, the DSF channel model is:

$$\mathbf{r} = \text{vec}(\mathbf{R}) = \mathbf{H} \text{vec}(\mathbf{S}) + \text{vec}(\mathbf{N}) = \mathbf{H}\mathbf{s} + \mathbf{n}$$
 (7)

where $\operatorname{vec}(\cdot)$ is the vectorization operator in column-major order, $\boldsymbol{s} = \operatorname{vec}(\boldsymbol{S})$, $\boldsymbol{n} = \operatorname{vec}(\boldsymbol{N})$, $\boldsymbol{H} \in \mathbb{C}^{N\beta \times N\beta}$ is the channel response matrix, and $\boldsymbol{N} \in \mathbb{C}^{\beta \times N}$ is the Gaussian noise matrix. \boldsymbol{H} has the form of [44]:

$$\boldsymbol{H} = \sum_{m=1}^{M} h_m \boldsymbol{T}_{\tau_m} \boldsymbol{\Delta}_{f_m} \tag{8}$$

where h_m is a complex Gaussian distributed fading factor, τ_m is the normalized delay and f_m is the normalized Doppler shift of the mth path. Furthermore, T_{τ_m} and Δ_{f_m} are expressed as:

$$m{T}_{ au_m} = egin{bmatrix} m{0} & m{I}_{ au_m} \\ m{I}_{Neta - au_m} & m{0} \end{bmatrix}$$
 (9a)

$$\Delta_{f_m} = \operatorname{diag}\left(\left[e^{\frac{j2\pi f_m \cdot l_{\text{CP}}}{N\beta}}, e^{\frac{j2\pi f_m \cdot (l_{\text{CP}}+1)}{N\beta}}, \dots, e^{\frac{j2\pi f_m \cdot (l_{\text{CP}}+N\beta-1)}{N\beta}}\right]\right)$$
(9b)

where I is the identity matrix, $\operatorname{diag}(\cdot)$ transforms a vector to a diagonal matrix, and $l_{\rm CP}$ is the length of CP. Assuming that rectangular pulses are transmitted, the input-output relationship of the transceiver is given by [44]:

$$\mathbf{w} = \text{vec}(\mathbf{W}) = (\mathbf{F}_N \otimes \mathbf{I}_{\beta})\mathbf{r} = (\mathbf{F}_N \otimes \mathbf{I}_{\beta})(\mathbf{H}\mathbf{s} + \mathbf{n})$$
$$= (\mathbf{F}_N \otimes \mathbf{I}_{\beta})(\mathbf{H}(\mathbf{F}_N^H \otimes \mathbf{I}_{\beta})\text{vec}(\mathbf{D}) + \mathbf{n}) = \tilde{\mathbf{H}}\mathbf{d} + \tilde{\mathbf{n}}$$
(10)

where \otimes is the Kronecker product, $(\cdot)^H$ denotes the Hermitian transpose, \mathbf{F}_N is the N-point DFT matrix, and

$$\boldsymbol{s} = (\boldsymbol{F}_N^H \otimes \boldsymbol{I}_\beta) \text{vec}(\boldsymbol{D}) \tag{11a}$$

$$\boldsymbol{d} = \operatorname{vec}(\boldsymbol{D}) = \operatorname{vec}(\boldsymbol{c}_r \boldsymbol{s}^T) = (\boldsymbol{I}_N \otimes \boldsymbol{c}_r) \boldsymbol{s}$$
 (11b)

$$[\mathbf{F}_N]_{n,n'} = \frac{1}{\sqrt{N}} e^{-\frac{j2\pi \cdot (n-1) \cdot (n'-1)}{N}}$$
 (11c)

$$\tilde{\boldsymbol{H}} = (\boldsymbol{F}_N \otimes \boldsymbol{I}_\beta) \boldsymbol{H} (\boldsymbol{F}_N^H \otimes \boldsymbol{I}_\beta)$$
 (11d)

$$\tilde{\boldsymbol{n}} = (\boldsymbol{F}_N \otimes \boldsymbol{I}_\beta)\boldsymbol{n} \tag{11e}$$

where $[\cdot]_{n,n'}$ denotes the (n,n') entry of a matrix. Since the receiver has access to the CSI, $\tilde{H} \in \mathbb{C}^{N\beta \times N\beta}$ is known. Although the size of \tilde{H} is large, according to (8), (9a), (9b), and (11d), \tilde{H} is sparse where large proportion of its entries are zeros [24]. Moreover, as per (2), the rank of original noise-free symbol matrix D is 1. Consequently, by exploiting the sparsity of \tilde{H} and the rank-1 property of D, the ADMM-based OTFS-DCSK signal detector is employed to recover the rank-1 matrix $C \in \mathbb{R}^{\beta \times N}$ from the received symbol matrix W, which will be detailed in next section. Each column vector of C represents a chaotic sequence, with the first one, c_0 , serving as the reference sequence, and the remaining ones being information-bearing sequences. Finally, the information symbol \bar{s}_n is obtained through chaotic demodulation as:

$$\bar{s}_n = \operatorname{sgn}\left(\boldsymbol{c}_0^T \cdot \boldsymbol{c}_n\right), \quad 1 \le n \le N - 1$$
 (12)

where $sgn(\cdot)$ is the sign function. The information bits are then decoded from the demodulated BPSK symbols.

III. ADMM-BASED OTFS-DCSK SIGNAL DETECTION

This section presents the proposed ADMM-based OTFS-DCSK signal detection algorithm. Specifically, ADMM is an optimization framework that decomposes complex problems into simpler subproblems, solving them iteratively to achieve convergence. It is particularly effective for structured optimization problems, making it suitable for OTFS-DCSK signal detection. The key steps involve updating primal variables by solving separate subproblems and adjusting the dual variable iteratively. This approach efficiently exploits the sparsity and structure of the OTFS channel response matrix, leading to improved detection performance.

According to (10), the target objective function is expressed as $\|\boldsymbol{w} - \tilde{\boldsymbol{H}}\boldsymbol{x}\|_2^2$ in the context of Gaussian noise, where $\|\cdot\|_2$ denotes the ℓ_2 -norm of a vector. Considering the constraints, as indicated in (11b), vectorizing \boldsymbol{D} results in \boldsymbol{d} , where \boldsymbol{D} is a real rank-1 matrix. Consequently, the real vector \boldsymbol{x} should represent the vectorized form of a rank-1 matrix, for instance, $\boldsymbol{x} = \text{vec}(\boldsymbol{u}\boldsymbol{v}^T) \in \mathbb{R}^{N\beta}$. With these considerations, we establish the optimization problem based on (11d) as:

$$\min_{\boldsymbol{x}, \boldsymbol{u}, \boldsymbol{v}} \|\boldsymbol{w} - \tilde{\boldsymbol{H}} \boldsymbol{x}\|_{2}^{2} \quad \text{s.t. } \boldsymbol{x} = \text{vec}(\boldsymbol{u} \boldsymbol{v}^{T})$$
 (13)

where $\boldsymbol{u} \in \mathbb{R}^{\beta}$, $\boldsymbol{v} \in \mathbb{R}^{N}$ and \boldsymbol{x} are primal variables for solving the optimization problem. Since real symbols are used for BPSK and both \boldsymbol{w} and $\tilde{\boldsymbol{H}}$ are complex, to accelerate computation and restrict the detected \boldsymbol{x} to a real-valued vector, we can convert \boldsymbol{w} and $\tilde{\boldsymbol{H}}$ into real-valued forms when BPSK symbols are transmitted, as follows:

$$\bar{\boldsymbol{w}} = \begin{bmatrix} \Re(\boldsymbol{w}) \\ \Im(\boldsymbol{w}) \end{bmatrix}$$
 (14a) $\bar{\boldsymbol{H}} = \begin{bmatrix} \Re(\tilde{\boldsymbol{H}}) \\ \Im(\tilde{\boldsymbol{H}}) \end{bmatrix}$ (14b)

where $\Re(\cdot)$ takes real parts of complex numbers and $\Im(\cdot)$ takes imaginary parts. Then (13) is equivalent to:

$$\min_{\boldsymbol{x}, \boldsymbol{y}, \boldsymbol{y}} \|\bar{\boldsymbol{w}} - \bar{\boldsymbol{H}} \boldsymbol{x}\|_2^2 \quad \text{s.t. } \boldsymbol{x} = \text{vec}(\boldsymbol{u} \boldsymbol{v}^T). \tag{15}$$

The augmented Lagrangian for (15) is constructed as:

$$L_{\rho}(\boldsymbol{x}, \boldsymbol{z}, \boldsymbol{\lambda}) = \|\bar{\boldsymbol{w}} - \bar{\boldsymbol{H}}\boldsymbol{x}\|_{2}^{2} + \boldsymbol{\lambda}^{T}(\boldsymbol{x} - \boldsymbol{z}) + \frac{\rho}{2}\|\boldsymbol{x} - \boldsymbol{z}\|_{2}^{2}$$
 (16)

where $z = \text{vec}(\boldsymbol{u}\boldsymbol{v}^T)$ is also the primal variable to be optimized in ADMM, λ is the dual Lagrange multiplier vector and $\rho > 0$ is the penalty parameter. The introduction of ρ in (16) ensures better numerical stability and convergence properties. A well-chosen ρ accelerates convergence by appropriately scaling the augmented Lagrangian terms, preventing slow updates and oscillations in the iterative process. In particular, ρ influences the step size of the primal and dual updates, allowing the algorithm to efficiently enforce the equality constraints while maintaining robustness in noisy environments. Subsequently, the general ADMM process is depicted as:

$$\boldsymbol{x}^{l+1} = \arg\min_{\boldsymbol{x}} \left(\|\bar{\boldsymbol{w}} - \bar{\boldsymbol{H}}\boldsymbol{x}\|_{2}^{2} + \frac{\rho_{l}}{2} \|\boldsymbol{x} - \boldsymbol{z}^{l} + \frac{\boldsymbol{\lambda}^{l}}{\rho_{l}}\|_{2}^{2} \right)$$
(17a)

$$\boldsymbol{z}^{l+1} = \arg\min_{\boldsymbol{z}} \left(\frac{\rho_l}{2} \left\| \boldsymbol{x}^{l+1} - \boldsymbol{z} + \frac{\boldsymbol{\lambda}^l}{\rho_l} \right\|_2^2 \right)$$
(17b)

s.t. $\boldsymbol{z} = \text{vec}(\boldsymbol{u}\boldsymbol{v}^T)$

$$\boldsymbol{\lambda}^{l+1} = \boldsymbol{\lambda}^l + \rho_l(\boldsymbol{x}^{l+1} - \boldsymbol{z}^{l+1})$$
 (17c)

$$\rho_{l+1} = \mu \rho_l \tag{17d}$$

where l is the iteration number, and $\mu > 1$ is a constant.

Equation (17a) is a convex least squares (LS) problem, and the optimal solution is obtained by solving:

$$\nabla_{\boldsymbol{x}} L_{\rho_l}(\boldsymbol{x}, \boldsymbol{z}^l, \boldsymbol{\lambda}^l) = 2\bar{\boldsymbol{H}}^T \bar{\boldsymbol{H}} \boldsymbol{x} - 2\bar{\boldsymbol{H}}^T \bar{\boldsymbol{w}} + \rho_l \left(\boldsymbol{x} - \boldsymbol{z}^l + \frac{\boldsymbol{\lambda}^l}{\rho_l} \right) = 0$$
(18)

and then we have:

$$(2\bar{\boldsymbol{H}}^T\bar{\boldsymbol{H}} + \rho_l \boldsymbol{I})\boldsymbol{x} = 2\bar{\boldsymbol{H}}^T\bar{\boldsymbol{w}} + \rho_l \boldsymbol{z}^l - \boldsymbol{\lambda}^l.$$
 (19)

Since $2\bar{\boldsymbol{H}}^T\bar{\boldsymbol{H}} + \rho_l\boldsymbol{I}$ is sparse, the LS problem in (17a) can be solved by LSQR algorithm efficiently [42]. We evaluate

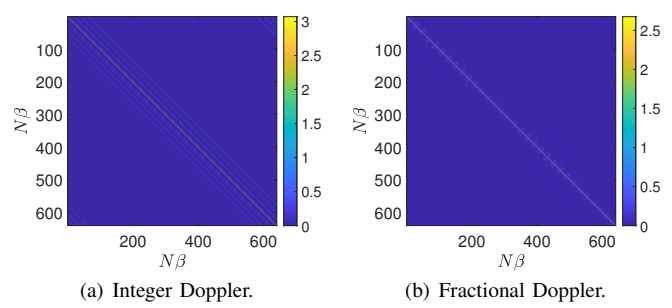


Fig. 3. Magnitudes of elements in $2\bar{\boldsymbol{H}}^T\bar{\boldsymbol{H}} + \rho_l \boldsymbol{I}$.

the sparsity of $2\bar{\pmb{H}}^T\bar{\pmb{H}}+\rho_l\pmb{I}$ by plotting the magnitudes of its elements, where Fig. 3(a) represents the integer Doppler case and Fig. 3(b) denotes the fractional Doppler case. The parameters are set as $N=32,~\beta=20,$ and the number of channel paths is 4. In the integer Doppler case, $\tau_m=f_m=m-1.$

In the fractional Doppler case, $\tau_m \sim \mathcal{U}\{1, 2, \dots, \beta - 1\}$ and $f_m \sim \mathcal{U}(0, f_{\text{max}})$ for $1 < m \leq M$, with $\tau_1 = f_1 = 0$, where $\mathcal{U}\{\cdot\}$ denotes the discrete uniform distribution and $\mathcal{U}(\cdot)$ represents the continuous one. The maximum normalized Doppler shift $f_{\rm max}$ is set to 0.5 in a system with a central frequency of 4 GHz, subcarrier spacing of 3.75 kHz, maximum speed of 506.25 km/h, and maximum Doppler shift of 1.875 kHz [45]. In both Figs. 3(a) and 3(b), most of elements have magnitudes nearly equal to 0, indicating the sparsity of $2\bar{H}^T\bar{H} + \rho_l I$ in both integer and fractional Doppler, demonstrating our applicability to both cases. Since $2\bar{\boldsymbol{H}}^T\bar{\boldsymbol{H}} + \rho_l \boldsymbol{I}$ is originated from $\bar{\boldsymbol{H}}$ in (14b), and $\bar{\boldsymbol{H}}$ is originated from $\tilde{\pmb{H}}$ in (11d), according to [44], only M elements in each row and column of \hat{H} have non-zero values, leading to the sparsity of $\bar{\boldsymbol{H}}$ and $2\bar{\boldsymbol{H}}^T\bar{\boldsymbol{H}} + \rho_l \boldsymbol{I}$. Moreover, the main diagonal elements represent the values of the main path, and the elements on remaining sub-diagonals in Fig. 3 correspond to the values of the other 3 paths. By utilizing the sparsity, the proposed ADMM algorithm efficiently detects signals across different paths and combines them to achieve maximum diversity gain, thereby mitigating the performance degradation caused by fading. Additionally, the dimensions of $2\bar{\boldsymbol{H}}^T\bar{\boldsymbol{H}}+\rho_l\boldsymbol{I}$ are $N\beta \times N\beta$, where $N\beta$ denotes the number of chaosmodulated chips in one OTFS-DCSK symbol. If N and β increase, the computational complexity becomes high when matrix sparsity is not exploited, leading to long latency in OTFS signal detection. Therefore, by leveraging the sparsity of $2\bar{\boldsymbol{H}}^T\bar{\boldsymbol{H}} + \rho_l \boldsymbol{I}$, our ADMM-based algorithm enables signal detection with acceptable complexity.

Since $z = \text{vec}(uv^T)$, we convert (17b) as:

$$oldsymbol{Z}^{l+1} = rg \min_{oldsymbol{Z}} \left(\left\| oldsymbol{X}_{oldsymbol{\lambda}^l,
ho_l}^{l+1} - oldsymbol{Z}
ight\|_F^2
ight)$$
 s.t. $oldsymbol{Z} = oldsymbol{u} oldsymbol{v}^T$

where $\|\cdot\|_F$ denotes the Frobenius norm, $\boldsymbol{X}_{\boldsymbol{\lambda}^l,\rho_l}^{l+1} = \operatorname{vec}_{\beta,N}^{-1}(\boldsymbol{x}^{l+1} + \boldsymbol{\lambda}^l/\rho_l)$ with $\operatorname{vec}^{-1}(\cdot)$ being the reverse process of vectorization whose subscript denotes the number of rows and columns of the resultant matrix, and $\boldsymbol{z}^{l+1} = \operatorname{vec}(\boldsymbol{Z}^{l+1})$. Subsequently, truncated SVD is applied to solve (20):

$$\boldsymbol{Z}_{*}^{l+1} = \sigma_{l+1,1} \boldsymbol{u}_{1}^{l+1} (\boldsymbol{v}_{1}^{l+1})^{T}$$
 (21)

where $\sigma_{l+1,1}$ denotes the largest singular value of $\boldsymbol{X}_{\boldsymbol{\lambda}^{l},\rho_{l}}^{l+1}$, and $\boldsymbol{u}_{1}^{l+1}, \boldsymbol{v}_{1}^{l+1}$ are its corresponding left and right singular vectors.

Algorithm 1 ADMM-based OTFS-DCSK Signal Detection Algorithm

- 1: **Input:** $\bar{\boldsymbol{H}}$, $\bar{\boldsymbol{w}}$, μ , maximum iteration number L
- 2: **Initialize:** Randomize \mathbf{x}^0 , \mathbf{z}^0 , $\boldsymbol{\lambda}^0$, and set $\rho_0 = 0.1$.
- 3: **for** $l = 0, 1, \dots, L-1$ **do**
- 4: **Update** x^{l+1} by using LSQR to solve (19).
- 5: Update z^{l+1} by using truncated SVD to solve (20).
- 6: **Update** λ^{l+1} based on (17c).
- 7: **Update** ρ_{l+1} based on (17d).
- 8: end for
- 9: Output: \boldsymbol{x}^L

After determining \boldsymbol{x}^{l+1} and \boldsymbol{z}^{l+1} , $\boldsymbol{\lambda}^{l+1}$ is updated by (17c),

and the ADMM-based algorithm is summarized in Algorithm 1. \boldsymbol{C} is then generated by:

$$C = \operatorname{vec}_{\beta N}^{-1}(\boldsymbol{x}^L) = [\boldsymbol{c}_0, \dots, \boldsymbol{c}_n, \dots, \boldsymbol{c}_{N-1}] \in \mathbb{R}^{\beta \times N}.$$
 (22)

Since $\boldsymbol{x}^L \approx \boldsymbol{z}^L = \text{vec}(\boldsymbol{u}^L(\boldsymbol{v}^L)^T)$, \boldsymbol{C} can be also approximated as a rank-1 matrix, denoted as $\boldsymbol{C} \approx \hat{\boldsymbol{c}}_r \hat{\boldsymbol{s}}_c^T = [\hat{s}_{c,0}\hat{\boldsymbol{c}}_r, \dots, \hat{s}_{c,n}\hat{\boldsymbol{c}}_r, \dots, \hat{s}_{c,N-1}\hat{\boldsymbol{c}}_r]$ where $\hat{\boldsymbol{c}}_r \in \mathbb{R}^\beta$ is the estimated chaos sequence, $\boldsymbol{c}_n = \hat{s}_{c,n}\hat{\boldsymbol{c}}_r$, and $\hat{\boldsymbol{s}}_c = [\hat{s}_{c,0}, \dots, \hat{s}_{c,n}, \dots, \hat{s}_{c,N-1}]^T \in \mathbb{R}^N$ is a continuous real-valued information-bearing vector. After the signal detection, \boldsymbol{C} is processed by chaos modulation and BPSK demodulation to decode the information bits.

IV. THEORETICAL ANALYSIS

A. Convergence

The convergence results of Algorithm 1 are summarized in the following theorem.

Theorem 1. Let $\{x^l, z^l, \lambda^l\}$ be the sequence generated by Algorithm 1. We have the following convergence properties [46]:

- (i) The generated sequences $\{x^l, z^l, \lambda^l\}$ generated by Algorithm 1 remain bounded throughout the iterative process, ensuring stability and numerical robustness of the updating procedure.
- (ii) The limit point {x*, z*, λ*} obtained by the algorithm is a stationary point satisfying the Karush-Kuhn-Tucker (KKT) conditions for the optimization problem in (15). This guarantees that Algorithm 1 converges toward an optimal or locally optimal solution, reflecting its reliability and effectiveness in solving the formulated signal detection problem.

Proof: See Appendix A.

B. Bit Error Rate and Diversity over DSF Channel

In this section, we derive BER and diversity in the presence of additive white Gaussian noise (AWGN) over DSF channel. The channel considered here exhibits DSF with each path having the independent and identically distributed (i.i.d.) $h_m \sim \mathcal{CN}(0,1/M)$, indicating equal average power of 1/M across all paths and $\sum_{m=1}^M \mathbb{E}[|h_m|^2] = 1$. Here \mathcal{CN} denotes complex Gaussian random variable and $\mathbb{E}[\cdot]$ is the expectation operator.

1) BER: We follow [39] to derive the BER for the proposed OTFS-DCSK transceiver over DSF channel. The cosine of the angle θ between estimated chaos sequence $\hat{\boldsymbol{c}}_r$ and chaos reference sequence \boldsymbol{c}_r is first computed as $\cos\theta = |\hat{\boldsymbol{c}}_r^T \boldsymbol{c}_r|/(\|\hat{\boldsymbol{c}}_r\|_2 \|\boldsymbol{c}_r\|_2)$ where $|\cdot|$ is the modulus of a complex number, and the length of projection of \boldsymbol{c}_r onto $\hat{\boldsymbol{c}}_r$

is $d_{c_r\hat{c}_r} = \cos\theta\sqrt{\beta\mathbb{E}[x_k^2]}$. Subsequently, the error probability of the decoded BPSK symbols is calculated as:

$$P(\hat{s}_{n} \neq s_{n} | \boldsymbol{h}, \theta) = Q\left(\frac{d_{\boldsymbol{c}_{r}\hat{\boldsymbol{c}}_{r}}}{\sigma}\right) = Q\left(\cos\theta\sqrt{\frac{\|\boldsymbol{h}\|_{2}^{2}\beta\mathbb{E}[x_{k}^{2}]}{N_{0}/2}}\right)$$

$$= Q\left(\cos\theta\sqrt{\frac{\|\boldsymbol{h}\|_{2}^{2}\beta/2}{N_{0}/2}}\right) = Q\left(\cos\theta\sqrt{\frac{\|\boldsymbol{h}\|_{2}^{2}\beta}{N_{0}}}\right)$$

$$= Q\left(\cos\theta\sqrt{\frac{2\|\boldsymbol{h}\|_{2}^{2}(N-1)E_{b}}{NN_{0}}}\right).$$
(23)

where \hat{s}_n is the nth element of the estimated BPSK symbol vector \hat{s} , $\hat{s} = \text{sgn}(\hat{s}_c) \in \mathbb{R}^N$ contains the decoded BPSK symbols, $N_0 = 2\sigma^2$ with σ^2 being the variance of AWGN, $\mathbb{E}[x_k^2] = 1/2$, $Q(x) = \int_x^\infty \exp(-t^2/2) dt$ is the Q-function, $E_b = (N\beta \mathbb{E}[x_k^2])/(N-1)$ is the energy cost per bit, and $h = [h_1, \ldots, h_M]^T \in \mathbb{C}^M$ is the i.i.d. complex Gaussian random vector containing channel fading factors for all paths [23], [47], [48]. (23) reveals the relationship between the symbol error rate and E_b/N_0 , which extends to the BER in BPSK modulation, where the BER equals the symbol error rate. Additionally, since the right hand side of (23) does not depend on n, the subscript n can be omitted in the left hand side, and the average error probability of decoding \hat{s} is equal to the error rate when decoding a single \hat{s}_n .

According to Fig. 2, non-coherent chaos demodulation is applied to demodulate information symbols. This process, outlined in (12), leverages the rank-1 property of C and can be rewritten as [39]:

$$\bar{s}_n = \operatorname{sgn}\left((\hat{s}_{c,0}\hat{\boldsymbol{c}}_r)^T \cdot (\hat{s}_{c,n}\hat{\boldsymbol{c}}_r)\right)
= \operatorname{sgn}\left(\hat{s}_{c,0} \cdot \hat{s}_{c,n}\right) = \operatorname{sgn}\left(\hat{s}_{c,0}\right) \cdot \operatorname{sgn}\left(\hat{s}_{c,n}\right)
= \hat{s}_0\hat{s}_n, \ 1 \le n \le N - 1.$$
(24)

Due to BPSK modulation, only the signs of $\hat{s}_{c,n}$ influence the demodulation results. The error rate for a single information symbol \bar{s}_n is determined by the product of \hat{s}_0 and \hat{s}_n . Notably, even if both values have incorrect signs, the resultant information symbol is correctly demodulated. Errors occur only when one of \hat{s}_0 or \hat{s}_n is incorrectly signed. Moreover, (23) shows that the error probability of the decoded BPSK symbols $P(\hat{s}_n \neq s_n | \boldsymbol{h}, \theta)$ is independent of the symbol index n. Therefore, $P(\hat{s}_0 \neq 1 | \boldsymbol{h}, \theta) = P(\hat{s}_n \neq s_n | \boldsymbol{h}, \theta)$ for all n where $s_0 = 1$, and the index n can be omitted. Subsequently, given specific θ and \boldsymbol{h} , the error rate for an information symbol \bar{s}_n is calculated as:

$$P_{e|\mathbf{h},\theta} = \frac{1}{N-1} \sum_{n=1}^{N-1} \left[P(\hat{s}_0 \neq 1 | \mathbf{h}, \theta) \left(1 - P(\hat{s}_n \neq s_n | \mathbf{h}, \theta) \right) + \left(1 - P(\hat{s}_0 \neq 1 | \mathbf{h}, \theta) \right) P(\hat{s}_n \neq s_n | \mathbf{h}, \theta) \right]$$

$$= 2P(\hat{s} \neq s | \mathbf{h}, \theta) \left(1 - P(\hat{s} \neq s | \mathbf{h}, \theta) \right)$$
(25)

where $s_0 = 1$ denotes the reference symbol. Since the channel model defined in (7) and (8) are quasi-static [44] and the corresponding parameters are randomly and independently defined,

the channel matrix \boldsymbol{H} already incorporates temporal variation through the Doppler shift operators. Each OTFS frame has a distinct \boldsymbol{H} , with its entries h_m being random variables. We then average the results over numerous independent OTFS frames to account for the time variability, as the Doppler effects are embedded in \boldsymbol{H} . Therefore, the BER in the presence of AWGN over DSF channel is determined numerically by calculating the expected value of $P_{e|\boldsymbol{h},\theta}$ across the permissible ranges of $\{\boldsymbol{h},\theta\}$ [40, Sec. IV-A, p. 7], [49, (10.107)], expressed as:

BER_{DSF} =
$$\mathbb{E}\left[P_{e|\boldsymbol{h},\theta}|\boldsymbol{h},\theta\right]$$

= $\mathbb{E}\left[2Q\left(\cos\theta\sqrt{\frac{2\|\boldsymbol{h}\|_{2}^{2}(N-1)E_{b}}{NN_{0}}}\right)\right]$ (26)
 $\times\left(1-Q\left(\cos\theta\sqrt{\frac{2\|\boldsymbol{h}\|_{2}^{2}(N-1)E_{b}}{NN_{0}}}\right)\right)\left|\boldsymbol{h},\theta\right|$

where the expectation is taken over the joint distribution of the fading coefficient vector \boldsymbol{h} and phase interval θ . (26) incorporates the Q-function, which accounts for symbol error probability given the channel conditions. This framework ensures BER evaluation under realistic channel conditions, even though a closed-form solution is unavailable due to the inherent complexity of integrating over the joint distributions of \boldsymbol{h} and θ . The numerical evaluation of these expectations allows for an accurate BER assessment under various fading conditions. Note that (26) is also applicable to both integer and fractional Doppler shift cases.

Note that in the derived BER expressions of (23) and (26), the BER is not explicitly dependent on the parameter β . Although $\cos\theta$ in (23) is computed based on the length- β transmitted reference sequence \mathbf{c}_r and the received reference sequence $\hat{\mathbf{c}}_r$, the power of both sequences is normalized in the computation of $\cos\theta = |\hat{\mathbf{c}}_r^T \mathbf{c}_r|/(\|\hat{\mathbf{c}}_r\|_2 \|\mathbf{c}_r\|_2)$, implying that β has minimal influence on the determination of $\cos\theta$. Therefore, we conclude that according to (23) and (26), the BER is not sensitive to β .

This behavior differs from conventional DCSK-based systems because our OTFS-DCSK framework incorporates rank-1 matrix approximation technique. According to (24), the dimension of correlation demodulation is reduced from vector-level operations in the former DCSK to symbol-level operations in the rank-1 matrix approximation-based DCSK. This dimensionality reduction helps decrease the number of summation terms in the BER expression, thereby eliminating the dependence on β .

2) Diversity: The received signal in (10) can be rewritten based on (8), (11b), (11d) as:

$$\mathbf{w} = \tilde{\mathbf{H}}\mathbf{d} + \tilde{\mathbf{n}} = \tilde{\mathbf{H}} (\mathbf{I}_{N} \otimes \mathbf{c}_{r}) \mathbf{s} + \tilde{\mathbf{n}}$$

$$= (\mathbf{F}_{N} \otimes \mathbf{I}_{\beta}) \mathbf{H} (\mathbf{F}_{N}^{H} \otimes \mathbf{I}_{\beta}) (\mathbf{I}_{N} \otimes \mathbf{c}_{r}) \mathbf{s} + \tilde{\mathbf{n}}$$

$$= \sum_{m=1}^{M} h_{m} (\mathbf{F}_{N} \otimes \mathbf{I}_{\beta}) \mathbf{T}_{\tau_{m}} \Delta_{f_{m}} (\mathbf{F}_{N}^{H} \otimes \mathbf{I}_{\beta}) (\mathbf{I}_{N} \otimes \mathbf{c}_{r}) \mathbf{s} + \tilde{\mathbf{n}}$$

$$= \sum_{m=1}^{M} h_{m} \Xi_{m} \mathbf{s} + \tilde{\mathbf{n}} = \Phi(\mathbf{s}) \mathbf{h} + \tilde{\mathbf{n}}$$

$$= \mathbb{E} \left[Q \left(\sqrt{\frac{\tilde{\mathbf{h}}^{H} \Lambda \tilde{\mathbf{h}}}{2N_{0}}} \right) \middle| \tilde{\mathbf{h}} \right]$$

$$= \mathbb{E} \left[Q \left(\sqrt{\frac{2MN\beta |\tilde{h}_{1}|^{2}}{N_{0}}} \right) \middle| \tilde{\mathbf{h}} \right]$$

where $\Xi_m = (\boldsymbol{F}_N \otimes \boldsymbol{I}_{\beta}) \boldsymbol{T}_{\tau_m} \boldsymbol{\Delta}_{f_m} (\boldsymbol{F}_N^H \otimes \boldsymbol{I}_{\beta}) (\boldsymbol{I}_N \otimes \boldsymbol{c}_r)$, and $\boldsymbol{\Phi}(\boldsymbol{s}) = [\Xi_1 \boldsymbol{s}, \dots, \Xi_M \boldsymbol{s}]$. Subsequently, the conditional pairwise error probability (PEP) is [50]:

$$P(\mathbf{s} \to \hat{\mathbf{s}} | \mathbf{h}) = P\left(\|\mathbf{w} - \mathbf{\Phi}(\hat{\mathbf{s}})\|_{2}^{2} < \|\mathbf{w} - \mathbf{\Phi}(\mathbf{s})\|_{2}^{2} \middle| \mathbf{h} \right)$$

$$= Q\left(\frac{\| \left(\mathbf{\Phi}(\hat{\mathbf{s}}) - \mathbf{\Phi}(\mathbf{s}) \right) \mathbf{h} \|}{\sqrt{2N_{0}}} \right).$$
(28)

Using the Chernoff upper bound, the PEP is expressed as:

$$P(\boldsymbol{s} \to \hat{\boldsymbol{s}}) \le \mathbb{E}\left[e^{\frac{-\|\boldsymbol{\Phi}(\boldsymbol{\delta})\boldsymbol{h}\|^2}{4N_0}} \middle| \boldsymbol{h} \right]$$
(29)

where $\Phi(\delta) = \Phi(\hat{s}) - \Phi(s)$, and $\delta = \hat{s} - s$. Since $\|\Phi(\delta)h\|^2 = h^H \Phi^H(\delta)\Phi(\delta)h = h^H \Upsilon(\delta)h$ where $\Upsilon(\delta) = \Phi^H(\delta)\Phi(\delta)$ is a Hermitian matrix, we obtain the upper bound

$$P(\boldsymbol{s} \to \hat{\boldsymbol{s}}) \le \left(\prod_{\bar{o} \in \mathcal{J}(\boldsymbol{s}, \hat{\boldsymbol{s}})} \lambda_{\bar{o}}\right)^{-1} \left(\frac{1}{4N_0}\right)^{-r(\boldsymbol{s}, \hat{\boldsymbol{s}})}$$
(30)

where $\mathcal{J}(\boldsymbol{s}, \hat{\boldsymbol{s}})$ is the index set of nonzero eigenvalues $\lambda_{\bar{o}}$ of $\Upsilon(\boldsymbol{\delta})$, which has cardinality $|\mathcal{J}(\boldsymbol{s}, \hat{\boldsymbol{s}})| = r(\boldsymbol{s}, \hat{\boldsymbol{s}}) = \operatorname{rank}(\Upsilon(\boldsymbol{\delta}))$ where $\operatorname{rank}(\cdot)$ denotes the rank of a matrix. Finally, the diversity of the proposed approach is

$$\operatorname{div} \triangleq \min_{\boldsymbol{s} \neq \hat{\boldsymbol{s}}} r(\boldsymbol{s}, \hat{\boldsymbol{s}}) \tag{31}$$

whose maximum value is M.

Employing (28) and substituting $\Phi(\delta) = \Phi(\hat{s}) - \Phi(s)$ as well as $\Upsilon(\delta) = \Phi^H(\delta)\Phi(\delta)$, the conditional PEP can be rewritten as:

$$P(\mathbf{s} \to \hat{\mathbf{s}} | \mathbf{h}) = Q\left(\sqrt{\frac{\|\mathbf{\Phi}(\mathbf{\delta})\mathbf{h}\|^2}{2N_0}}\right)$$

$$= Q\left(\sqrt{\frac{\mathbf{h}^H \mathbf{\Phi}^H(\mathbf{\delta})\mathbf{\Phi}(\mathbf{\delta})\mathbf{h}}{2N_0}}\right) = Q\left(\sqrt{\frac{\mathbf{h}^H \mathbf{\Upsilon}(\mathbf{\delta})\mathbf{h}}{2N_0}}\right). \tag{32}$$

Subsequently, the PEP is obtained by calculating the expected value of the conditional probability over all realizations of h, expressed as:

$$P(\mathbf{s} \to \hat{\mathbf{s}}) = \mathbb{E}\left[Q\left(\sqrt{\frac{\mathbf{h}^H \Upsilon(\mathbf{\delta})\mathbf{h}}{2N_0}}\right) \middle| \mathbf{h} \right].$$
 (33)

Expressing the Hermitian matrix $\Upsilon(\delta)$ with the use of eigenvalue decomposition as $U^H \Lambda U$, where U is the eigenvector matrix, and $\Lambda = \text{diag}\{\lambda_1, \dots, \lambda_{\bar{o}}, \dots, \lambda_{\bar{O}}\}$ is the diagonal eigenvalue matrix, the PEP is derived as [45]:

$$P(\mathbf{s} \to \hat{\mathbf{s}}) = \mathbb{E} \left[Q \left(\sqrt{\frac{\mathbf{h}^H \mathbf{U}^H \mathbf{\Lambda} \mathbf{U} \mathbf{h}}{2N_0}} \right) \middle| \mathbf{h} \right]$$

$$= \mathbb{E} \left[Q \left(\sqrt{\frac{\tilde{\mathbf{h}}^H \mathbf{\Lambda} \tilde{\mathbf{h}}}{2N_0}} \right) \middle| \tilde{\mathbf{h}} \right]$$

$$= \mathbb{E} \left[Q \left(\sqrt{\frac{2MN\beta |\tilde{h}_1|^2}{N_0}} \right) \middle| \tilde{h}_1 \right] = \frac{1}{2} \left(1 - \sqrt{\frac{N\beta}{N\beta + N_0}} \right)$$
(34)

where $\tilde{\boldsymbol{h}} = \boldsymbol{U}\boldsymbol{h} = [\tilde{h}_1, \cdots, \tilde{h}_m, \cdots, \tilde{h}_M]$, with $\tilde{h}_m \sim \mathcal{CN}(0, 1/M)$. Finally, the BER lower bound can be calculated according to [45] as:

BER
$$\geq \frac{1}{2^{N\beta}} \sum_{a=1}^{\alpha} P(\boldsymbol{s} \to \hat{\boldsymbol{s}}) = \frac{\alpha}{2^{N\beta}} \frac{1}{2} \left(1 - \sqrt{\frac{N\beta}{N\beta + N_0}} \right)$$

where α is the number of $\Upsilon(\delta)$ having rank one.

C. Spectral Efficiency

In this section, we investigate the spectral efficiency of multiple binary multi-carrier DCSK systems to highlight the OTFS-DCSK superiority. For simplicity, we assume that one multi-carrier symbol without CP is transmitted in unit time, ensuring that each subcarrier occupies unit bandwidth. To combat fading, a CP of length $l_{\rm CP}$ is added to all multi-carrier DCSK systems. The CP length should exceed the maximum number of delayed symbols, i.e., $l_{\rm CP} > \tau_{\rm max}$, where $\tau_{\rm max}$ represents the maximum path delay in a DSF channel.

In the case of OTFS-DCSK-based systems, only one CP is required for the transmission of N chaos sequences of length β [24]. This means that a CP with length $l_{\rm CP}$ can serve the $N\beta$ resource blocks in the TF domain, significantly reducing the required length of the CP. The spectral efficiency upper bound (SEUB) of OTFS-DCSK is calculated as:

$$SEUB_{OTFS-DCSK} = \frac{N-1}{N\beta + l_{CP}}.$$
 (36)

where the actual spectral efficiency depends on the signal-tonoise ratio and other system impairments, which influence the achievable data rate. (36) represents only the theoretical upper bound of spectral efficiency, assuming ideal transmission conditions without considering the impact of noise, interference, or imperfect channel estimation.

For the conventional OFDM-DCSK system [15], N subcarriers and β chaos chips are required to carry N-1 bits. Additionally, the CP is added β times to each OFDM symbol to combat fading. Therefore, the SEUB of OFDM-DCSK is:

$$SEUB_{OFDM-DCSK} = \frac{N-1}{(N+l_{CP})\beta}$$
 (37)

With this baseline established, index modulation-based multicarrier DCSK systems [51], [52] can transmit more bits, necessitating adjustments to the number of subcarriers in some systems. These result in changes to the value of N-1 in the numerator and N in the denominator of (37).

It can be concluded from (36) and (37) that OTFS-DCSK has higher SEUB than that of OFDM-DCSK since the requirement of CP is reduced. We should emphasize that this value is applicable for OTFS-DCSK systems where the $N\beta$ resource blocks in the TF domain carry only one reference chaos sequence. Both the SVD-based OTFS-DCSK system [38] and the proposed approach meet this requirement. An exception is found in [37], where $2N\beta$ resource blocks in the TF domain are used to carry N reference sequences. This overuse of reference sequences results in a lower SEUB compared to those of [38] and our solution.

TABLE I SEUB COMPARISON AMONG MULTI-CARRIER DCSK SYSTEMS

System	SEUB
OFDM-DCSK [15]	$\frac{N-1}{(N+l_{\mathrm{CP}})\beta}$
SVP-OFDM-DCSK [21]	$\frac{N-1}{(N+l_{\mathrm{CP}})\beta}$
Carrier index MC-DCSK [51]	$\frac{N-1+\log_2 N}{(N+1+l_{\rm CP})\beta}$
EECI-OFDM-DCSK [52]	$\frac{N-1+(\log_2 N)-1}{(N+l_{\rm CP})\beta}$
MRC-OTFS-DCSK [37]	$\frac{N}{2N\beta+l_{\mathrm{CP}}}$
SVD-OTFS-DCSK [38]	$\frac{N-1}{N\beta+l_{\mathrm{CP}}}$
Proposed	$\frac{N-1}{N\beta+l_{\mathrm{CP}}}$

Table I compares the SEUB between the proposed and other binary multi-carrier DCSK-based systems.

D. Complexity

The complexity of the proposed approach primarily originates from the LSOR process, due to the involvement of the large matrix $2\bar{\pmb{H}}^T\bar{\pmb{H}}+\rho_l\pmb{I}$ in solving the LS problem. The complexity of the LSQR algorithm is related to its iteration number and the number of non-zero elements in a sparse matrix [53]. As shown in Fig. 3, in the integer Doppler case, the number of nonzero elements in $2\bar{\boldsymbol{H}}^T\bar{\boldsymbol{H}}+\rho_l\boldsymbol{I}$ is $(2M-1)N\beta$. In the fractional Doppler case, applying a threshold to set small-magnitude values to 0 results in a similar number of nonzero elements as in the integer Doppler case with minimal performance loss. Consequently, the complexity of executing one LSOR algorithm is $\mathcal{O}((2M-1)N\beta)$ when the iteration number of LSQR is kept low within the ADMM framework. Additionally, since LSQR is performed during the ADMM iterations, hence the overall complexity of the LSQR amounts to $\mathcal{O}(l_{\text{ADMM}}(2M-1)N\beta)$, where l_{ADMM} denotes the number of ADMM iterations. If the number of channel paths M is small, the complexity can be further reduced to $\mathcal{O}(l_{\text{ADMM}}N\beta)$. Moreover, since the complexity of a single execution of truncated SVD is $\mathcal{O}(N\beta)$, the overall complexity throughout the algorithm is $\mathcal{O}(l_{\text{ADMM}}N\beta)$. Subsequently, the total complexity of the proposed detector is the sum of the complexity of LSQR and truncated SVD, namely, $\mathcal{O}(l_{\text{ADMM}}2MN\beta).$

For other multi-carrier DCSK systems combating DSF, the singular vector pre-coded OFDM-DCSK (SVP-OFDM-DCSK) [21] must perform SVD on the full-rank $N \times N$ matrix, resulting in a complexity of $\mathcal{O}(N^3)$. Moreover, SVP-OFDM-DCSK requires sending the CSI to both the transmitter and receiver, whereas our solution only necessitates CSI at the receiver. The SVD-aided OTFS-DCSK [38] is also designed to address DSF, with a complexity of $\mathcal{O}(N\beta)$ since SVD is performed on the rank-1 $N \times \beta$ matrix. However, SVD-aided OTFS-DCSK is inferior to ours, which will be discussed in the following section. Table II compares the complexity of multi-carrier DCSK systems combating DSF.

V. SIMULATION RESULTS

Computer simulations are conducted to assess the performance of the proposed approach. A second-order CPF is

TABLE II
COMPLEXITY COMPARISON AMONG MULTI-CARRIER DCSK SYSTEMS
COMBATING DSF

System	Complexity
SVP-OFDM-DCSK [21]	$\mathcal{O}(N^3)$
SVD-OTFS-DCSK [38]	$\mathcal{O}(Neta)$
Proposed	$\mathcal{O}(l_{ ext{ADMM}}2MN\beta)$

employed for chaotic signal generation. The default parameters used in the simulation are introduced as follows. The system has N=32 subcarriers, and the chaotic sequence length is $\beta=20$. The E_b/N_0 range considered is [0,20] dB. For each E_b/N_0 value, over 500000 bits are involved to compute the BER. Unless otherwise stated, the DSF model follows (8), (9a), and (9b). The fading factors are distributed as $h_m \sim \mathcal{CN}(0,1/M)$, where M=4. The delay and Doppler shift are set as $\tau_m=f_m=m-1$, where m=1,2,3,4 [21]. The predefined set of parameters serves as a baseline configuration, ensuring consistency across different simulations. When analyzing the impact of a specific parameter, only that parameter is modified while the others remain unchanged.

A. Convergence of Algorithm

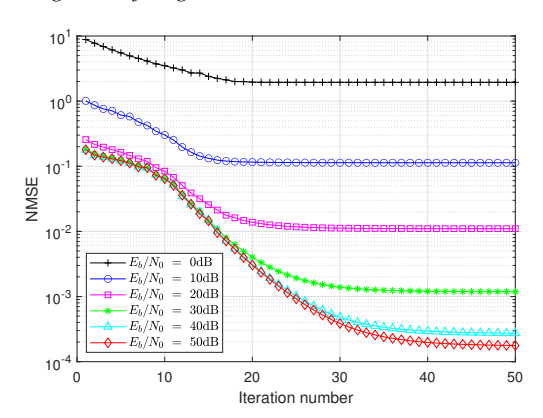


Fig. 4. NMSE versus iteration number.

Fig. 4 demonstrates the fast convergence of normalized mean square error (NMSE) over 50 iterations for various E_b/N_0 values, ranging from 0 dB to 50 dB. We adopt the NMSE to examine the convergence of algorithm, defined as:

$$NMSE = \mathbb{E}\left[\|\boldsymbol{C} - \boldsymbol{D}\|_F^2 / \|\boldsymbol{D}\|_F^2\right]$$
 (38)

The NMSE measures the discrepancy between the estimated rank-1 matrix \boldsymbol{C} and the transmitted noise-free rank-1 matrix \boldsymbol{D} in the DD domain. A lower NMSE indicates higher accuracy in signal reconstruction at the detector output. In Fig. 4, higher E_b/N_0 values lead to significantly lower NMSE, highlighting the beneficial impact of better signal quality on estimation accuracy. As the iteration number increases, the NMSE rapidly decreases across low E_b/N_0 values, demonstrating rapid convergence and effectiveness of the proposed algorithm in accurately estimating transmitted signals.

From Fig. 4, it is observed that as E_b/N_0 increases, more iterations are required for convergence. This phenomenon is closely related to the precision required by the algorithm. At

lower E_b/N_0 , the error level is relatively high, meaning that the algorithm can reach a stable solution quickly without excessive refinement. However, as E_b/N_0 increases, the overall error decreases, which implies that the algorithm must refine the solution to a much lower error level before convergence is deemed to be attained. It is important to note that the algorithm achieves a significantly low NMSE with high E_b/N_0 value, demonstrating its effectiveness in such scenarios. Additionally, in practical implementations, the stopping criterion can be adjusted to terminate iterations earlier when the performance improvement becomes marginal, balancing computational efficiency and accuracy.

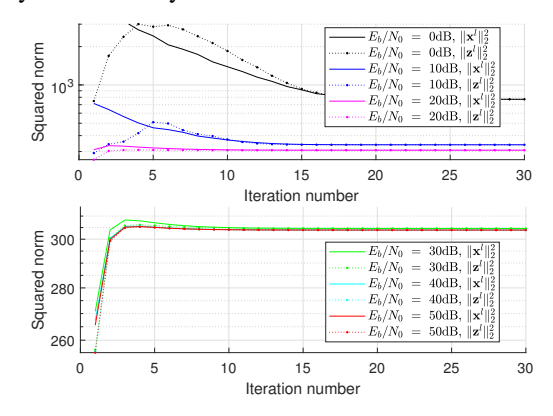


Fig. 5. Squared norm of variables versus iteration number.

Fig. 5 plots the values of $\|x^l\|$ and $\|z^l\|$ versus number of iterations. It is evident that these two norms converge to an identical value within a few iterations, demonstrating the fast convergence of the proposed ADMM-based OTFS-DCSK detector. Furthermore, it illustrates the bounded nature of x^l and z^l . The results are consistent across a wide range of $E_b/N_0 \in [0, 50]$ dB, showcasing the adaptability of our algorithm in combating noise.

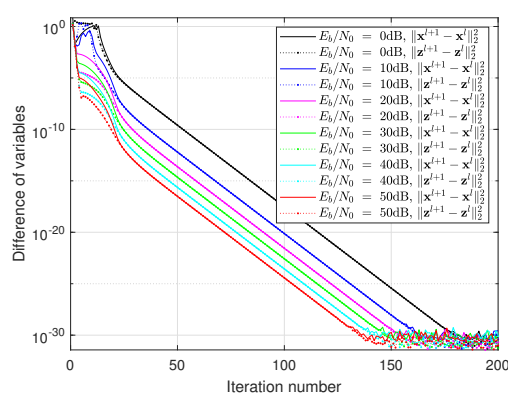


Fig. 6. Difference of variables versus iteration number.

Fig. 6 illustrates the convergence of \boldsymbol{x}^l and \boldsymbol{z}^l versus iteration number of Algorithm 1 without stopping criterion. We observe that as $l \to \infty$, both $\|\boldsymbol{x}^{l+1} - \boldsymbol{x}^l\|_2^2 \to 0$ and $\|\boldsymbol{z}^{l+1} - \boldsymbol{z}^l\|_2^2 \to 0$, indicating that the variables will ultimately converge. This trend holds across a wide E_b/N_0 range, from 0 dB to 50 dB. In scenarios with higher E_b/N_0 , the differences between variables are smaller. From 0 to 20 iterations, the difference of variables exhibits a rapid initial decline, followed by noticeable fluctuations, especially at low

 E_b/N_0 values. This behavior corresponds to the transient state in the iterative process, where the algorithm quickly reduces the large initial errors and adapts to the optimization constraints. The fluctuations occur because estimates still have relatively large adjustments, and noise in the system can have a more significant impact at this stage. Between 20 and 150 iterations, the changes of the estimates are relatively small. This phase corresponds to the steady state, where the updates become smaller as the algorithm moves toward an optimal solution. The convergence rate in this region follows a typical diminishing-step behavior observed in iterative optimization methods, where the magnitude of updates decreases progressively. It is important to note that due to the limits of computational precision, the difference value cannot be lower than 10^{-32} after over 150 iterations. Additionally, the trends of x^l and z^l align rapidly within a few iterations.

B. Running Time of Algorithm

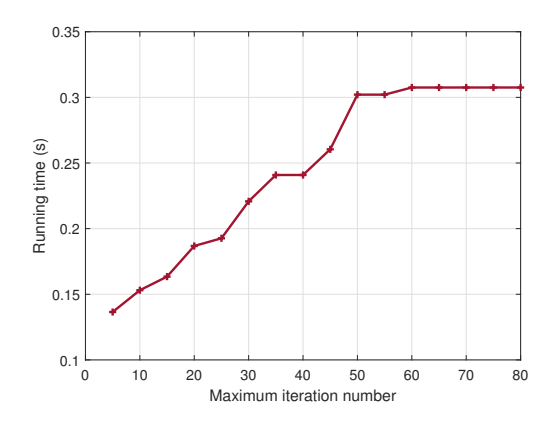


Fig. 7. Running time versus maximum iteration number of ADMM-based algorithm.

The running time versus maximum iteration number of the ADMM algorithm is shown in Fig. 7. In this simulation, E_b/N_0 is set to 10 dB, the number of subcarriers is N=32, the chaos sequence length is $\beta=32$, the number of channel paths is 4, and 1000 independent trials are conducted. Note that the algorithm will terminate before reaching the maximum iteration number if the stopping criterion is met. Initially, the running time grows approximately linearly, reflecting the computational cost during the iterations. However, beyond approximately 50 iterations, the running time begins to stabilize, indicating that the algorithm stopping criterion is met. That is, only around 50 iterations are needed and this suggests that the proposed scheme maintains reasonable computational complexity.

C. Signal-to-Noise Ratio (SNR) versus Velocity

Fig. 8 plots the SNR versus velocity. The parameters used are identical to those in the above test. Here, we consider a long-term evolution (LTE) system using Band 3, with a central frequency of 1.8 GHz and a subcarrier spacing of 15 kHz.

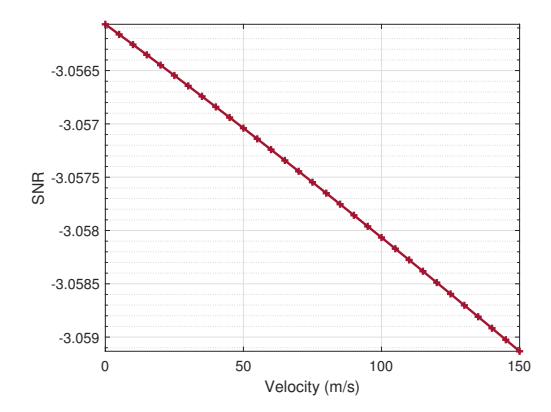


Fig. 8. SNR versus velocity.

In Fig. 8, we observe that SNR decreases slightly as velocity increases. Additionally, compared to the high E_b/N_0 value of 10 dB, the SNR is around -3 dB, significantly lower than E_b/N_0 . This is due to the adverse effects of channel impairment and the spreading process of chaos modulation. Furthermore, thanks to the spreading, SNR is only weakly affected by velocity, as indicated by the minimal decline in SNR with increasing velocity.

D. NMSE Comparison across Multi-Carrier DCSK Systems

In this study, the NMSE is calculated based on 1000 independent runs across various E_b/N_0 values. For comparison, we select two multi-carrier DCSK systems: SVP-OFDM-DCSK [21] and SVD-aided OTFS-DCSK [38], which are newly designed to combat DSF.

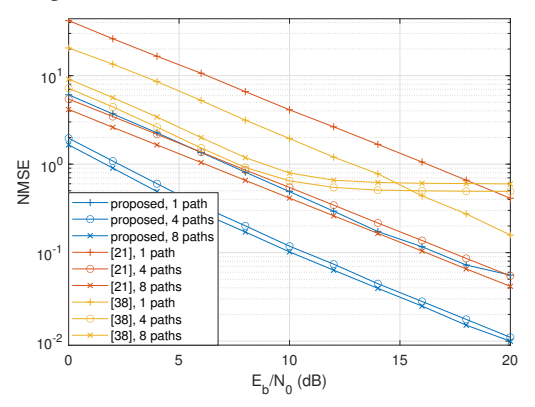


Fig. 9. NMSE versus E_b/N_0 at M=1,4,8.

Fig. 9 plots the NMSE results for various numbers of channel paths, with the delay and Doppler shift set as $\tau_m = f_m = m-1$, where $1 \leq m \leq M$. When M=1, $\tau_1 = f_1 = 0$, it becomes a flat fading channel. We observe that increasing the number of channel paths results in a lower NMSE for the proposed approach. This improvement is attributed to the effective utilization of sparsity and the rank-1 property of the system. Our system demonstrates lower NMSE compared to the other two systems under comparison. [38] struggles with M>1 because the received symbols affected by the channel response are not rank-1, and directly using SVD for demodulation does not yield good performance over DSF channels. Additionally, since [21] does not include noise reduction methods and its performance gain primarily comes

from the diversity gain obtained by decomposing the channel response matrix, it does not work well over flat fading channel. By contrast, the proposed approach maintains consistent performance over both flat and DSF channels, indicating its superior adaptability in combating various types of fading.

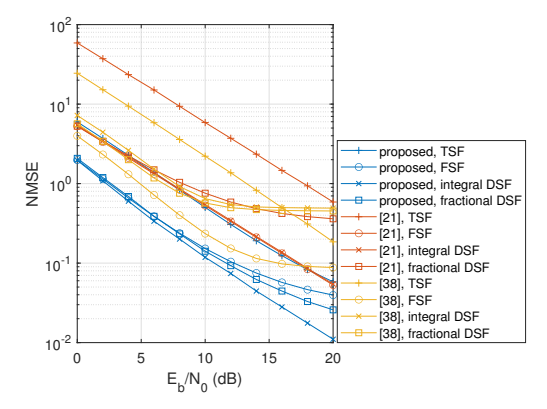


Fig. 10. NMSE over various fading channels.

Fig. 10 plots the NMSE over time-selective fading (TSF), frequency-selective fading (FSF), and DSF channels with integer and fractional Doppler shifts. For the TSF channel, we set M = 1, $\tau_1 = 0$, and $f_1 = 1$ while M = 4, $\tau_m=m-1$, and $f_m=0$ are assigned in the FSF channel. For fractional Doppler shift, we employ $\tau_m \sim \mathcal{U}\{1, 2, \dots, \beta - 1\}$ and $f_m \sim \mathcal{U}(0, 0.5)$ for $1 < m \le M$ [45], and $\tau_1 = f_1 = 0$. We see that the proposed approach achieves lower NMSE compared to [21] and [38], highlighting the former's superior detection accuracy. Additionally, the former attains the lowest NMSE over the DSF channel due to its highest diversity gain. In contrast, [38] performs poorly under TSF and DSF due to the loss of rank-1 property caused by Doppler shifts. Furthermore, we study the integral and fractional DSF cases in Fig. 10. It is observed that the NMSE values in both DSF cases are similar at low E_b/N_0 values, demonstrating the effectiveness of the proposed detection algorithm in handling both scenarios. This indicates that the algorithm can mitigate the challenges introduced by fractional Doppler shifts, ensuring stable performance even in the presence of fractional Doppler shifts.

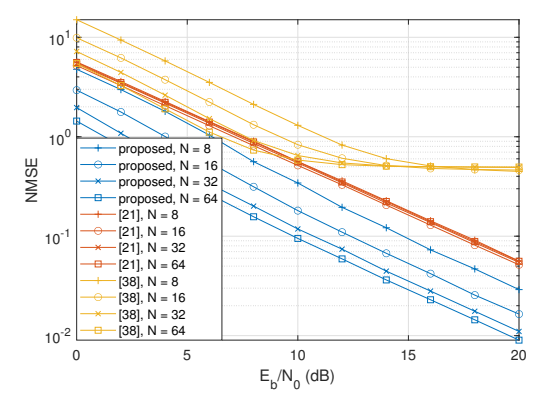


Fig. 11. NMSE versus E_b/N_0 at N = 8, 16, 32, 64.

Fig. 11 plots the NMSE results for different values of sub-carrier number N. We observe that our solution achieves significantly lower NMSE compared to other systems. Moreover,

as the number of subcarriers increases, the proposed approach continues to yield lower NMSE, whereas other systems do not fully leverage the increased N to enhance performance. This is because increasing the number of subcarriers enhances signal resolution in the DD domain, enabling OTFS to better mitigate multipath and Doppler effects in DSF channels, thereby increasing detection accuracy.

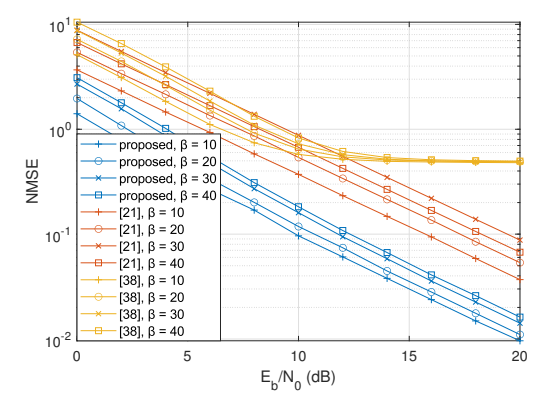


Fig. 12. NMSE versus E_b/N_0 at $\beta = 10, 20, 30, 40$.

Fig. 12 plots the NMSE for different chaos sequence lengths β . We see that the proposed approach consistently achieves lower NMSE compared to other systems, regardless of the value of β . In our solution, a longer chaos sequence results in a higher NMSE, indicating a trade-off between signal detection accuracy and chaotic key space. Moreover, the NMSE value does not change significantly with β , in contrast to the trends observed with the number of subcarriers N in Fig. 11.

E. BER Performance Comparison across Multi-Carrier DCSK Systems

The BER performance of the proposed approach is evaluated by comparing with [21] and [38]. For each E_b/N_0 value, over 500000 bits are simulated, thus the results are reliable for BER values above 10^{-5} .

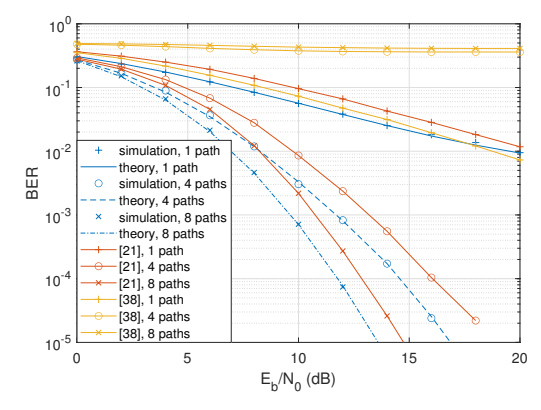


Fig. 13. BER versus E_b/N_0 at M=1,4,8.

Fig. 13 plots the BER results versus E_b/N_0 in different channels. For M=1, the channel exhibits flat fading. It is observed that the simulated BERs of our scheme closely match the analytical BERs derived in Section IV-B, corroborating our theoretical calculations. Moreover, as the number of channel paths increases, the proposed approach achieves a lower BER due to the increased channel diversity gain. Our

system outperforms [21] over fading channels regardless of the number of paths and [38] over DSF channels. In a flat fading channel, [38] is slightly superior to the proposed approach at high E_b/N_0 values. However, [38] struggles with symbol demodulation over DSF channels, resulting in its restricted applicability. Moreover, the diversity value is indicated by the slope of the BER curve. It is seen that these slopes for different numbers of paths are approximately equal to M, demonstrating that the proposed approach attains a high diversity gain.

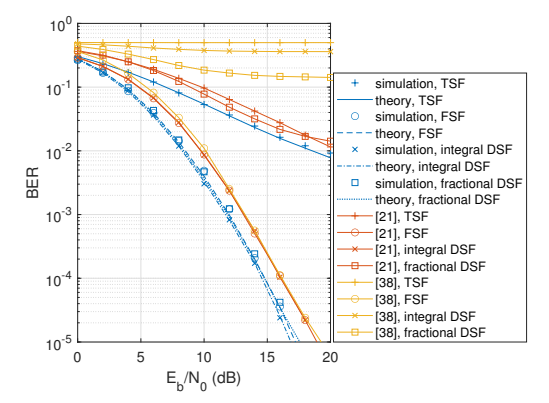


Fig. 14. BER over various fading channels.

Fig. 14 plots the BER over TSF, FSF, and DSF channels, where the DSF channel includes cases with integer and fractional Doppler shifts. We see that the proposed approach attains lower BER compared to [21] and [38], demonstrating the former superior reliability. Additionally, the simulated BER closely agrees with the analytical BER. The proposed approach exhibits low BER over FSF and DSF channels, as the diversity gain from multipath is fully exploited for BPSK demodulation. In contrast, [38] performs poorly over TSF and DSF channels due to the loss of the rank-1 property of the received symbol matrix. Furthermore, the results of integral and fractional DSF cases are plotted in Fig. 14. It is observed that the BER values for both DSF cases are similar, indicating that the proposed approach effectively mitigates the impact of fractional Doppler shifts. This suggests that the system is robust to fractional Doppler effects, ensuring reliable detection in practical scenarios where Doppler shifts are real-valued. Even in the fractional Doppler case, the derived theoretical BER matches the simulated BER well. The close agreement between theoretical and simulated BER curves further confirms the accuracy of the analytical derivation.

Fig. 15 illustrates the BER at different values of subcarrier number N. We observe that the proposed approach achieves significantly lower BER as N increases. This is because a larger N allows for a better resolution in the DD domain, which enhances the ability to combat multipath effects and Doppler spread. However, as N increases, the computational complexity of the system also grows, requiring a trade-off between performance and complexity. Even though when N=8, the proposed approach does not outperform the competitors in all cases, it shows better BER performance as N increases to 16, 32, and 64, demonstrating its effectiveness in mitigating DSF. Moreover, [21] does not perform better with

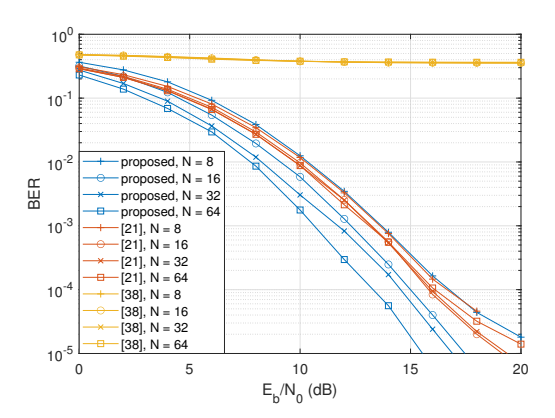


Fig. 15. BER versus E_b/N_0 at N = 8, 16, 32, 64.

a larger N, and [38] fails to demodulate the symbols over DSF channel.

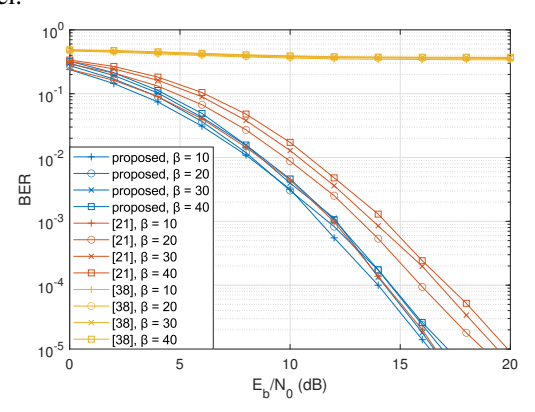


Fig. 16. BER versus E_b/N_0 at $\beta = 10, 20, 30, 40$.

Fig. 16 plots the BER versus chaos sequence length β . The proposed approach shows insensitivity to β , with BER values remaining similar over a wide range of $\beta=10,20,30,40$. This robustness can be attributed to the inherent properties of the OTFS modulation scheme, which effectively mitigates the effects of DSF channels. The insensitivity to β implies that the OTFS-DCSK system can achieve reliable communication without the need to frequently adjust the spreading factor, simplifying system design and implementation. In contrast, [21] exhibits a low BER at $\beta=10$, but its value increases rapidly as β grows. Additionally, the system in [38] does not perform well over DSF channel, as the received matrix is no longer rank-1.

VI. CONCLUSION

This paper proposes an ADMM-based detection algorithm for OTFS-DCSK systems to enhance reliability in high-mobility scenarios, effectively combating DSF and noise. By exploiting channel sparsity and the rank-1 structure of transmitted symbols, the proposed method integrates LSQR and truncated SVD for efficient detection. The chaotic spreading property of DCSK further enhances resistance to interception and jamming. Convergence speed, BER performance, spectral efficiency, diversity gain, and complexity are analyzed. Simulation results verify rapid convergence, robust performance under fractional Doppler shifts, and superior reliability com-

pared to existing multi-carrier DCSK schemes, confirming its practicality for high-mobility communications.

APPENDIX A PROOF OF THEOREM 1

The proof is motivated by [46] which focuses on tensor completion, while this paper concentrates on matrix approximation. The updates of $\{\boldsymbol{x}^{l+1}, \boldsymbol{z}^{l+1}, \boldsymbol{\lambda}^{l+1}, \rho_{l+1}\}$ during the lth iteration are represented by the updates in (16). The augmented Lagrangian function after the lth iteration is:

$$L_{\rho_{l}}(\boldsymbol{x}^{l}, \boldsymbol{z}^{l}, \boldsymbol{\lambda}^{l})$$

$$= \|\bar{\boldsymbol{w}} - \bar{\boldsymbol{H}}\boldsymbol{x}^{l}\|_{2}^{2} + \boldsymbol{\lambda}^{l}(\boldsymbol{x}^{l} - \boldsymbol{z}^{l}) + \frac{\rho_{l}}{2}\|\boldsymbol{x}^{l} - \boldsymbol{z}^{l}\|_{2}^{2}$$

$$= \|\bar{\boldsymbol{w}} - \bar{\boldsymbol{H}}\boldsymbol{x}^{l}\|_{2}^{2} + \frac{\rho_{l}}{2}\|\boldsymbol{x}^{l} - \boldsymbol{z}^{l} + \frac{\boldsymbol{\lambda}^{l}}{\rho_{l}}\|_{2}^{2} - \frac{\rho_{l}}{2}\|\frac{\boldsymbol{\lambda}^{l}}{\rho_{l}}\|_{2}^{2}.$$
(39)

Subsequently, after updating $\{x^{l+1}, z^{l+1}, \lambda^{l+1}, \rho_{l+1}\}$, the augmented Lagrangian becomes:

$$L_{\rho_{l}}(\boldsymbol{x}^{l+1}, \boldsymbol{z}^{l}, \boldsymbol{\lambda}^{l}) = \|\bar{\boldsymbol{w}} - \bar{\boldsymbol{H}}\boldsymbol{x}^{l+1}\|_{2}^{2} + \boldsymbol{\lambda}^{lT}(\boldsymbol{x}^{l+1} - \boldsymbol{z}^{l}) + \frac{\rho_{l}}{2}\|\boldsymbol{x}^{l+1} - \boldsymbol{z}^{l}\|_{2}^{2}$$

$$= \|\bar{\boldsymbol{w}} - \bar{\boldsymbol{H}}\boldsymbol{x}^{l+1}\|_{2}^{2} + \frac{\rho_{l}}{2}\|\boldsymbol{x}^{l+1} - \boldsymbol{z}^{l} + \frac{\boldsymbol{\lambda}^{l}}{\rho_{l}}\|_{2}^{2} - \frac{\rho_{l}}{2}\|\frac{\boldsymbol{\lambda}^{l}}{\rho_{l}}\|_{2}^{2}$$

$$L_{\rho_{l}}(\boldsymbol{x}^{l+1}, \boldsymbol{z}^{l+1}, \boldsymbol{\lambda}^{l})$$

$$= \|\bar{\boldsymbol{w}} - \bar{\boldsymbol{H}}\boldsymbol{x}^{l+1}\|_{2}^{2} + \boldsymbol{\lambda}^{lT}(\boldsymbol{x}^{l+1} - \boldsymbol{z}^{l+1}) + \frac{\rho_{l}}{2}\|\boldsymbol{x}^{l+1} - \boldsymbol{z}^{l+1}\|_{2}^{2}$$

$$= \|\bar{\boldsymbol{w}} - \bar{\boldsymbol{H}}\boldsymbol{x}^{l+1}\|_{2}^{2} + \frac{\rho_{l}}{2}\|\boldsymbol{x}^{l+1} - \boldsymbol{z}^{l+1} + \frac{\boldsymbol{\lambda}^{l}}{\rho_{l}}\|_{2}^{2} - \frac{\rho_{l}}{2}\|\frac{\boldsymbol{\lambda}^{l}}{\rho_{l}}\|_{2}^{2}$$

$$= \|\bar{\boldsymbol{w}} - \bar{\boldsymbol{H}}\boldsymbol{x}^{l+1}\|_{2}^{2} + \frac{\rho_{l}}{2}\|\boldsymbol{x}^{l+1} - \boldsymbol{z}^{l+1} + \frac{\boldsymbol{\lambda}^{l+1}}{\rho_{l}}\| + \frac{\rho_{l}}{2}\|\boldsymbol{x}^{l+1} - \boldsymbol{z}^{l+1}\|_{2}^{2}$$

$$= \|\bar{\boldsymbol{w}} - \bar{\boldsymbol{H}}\boldsymbol{x}^{l+1}\|_{2}^{2} + \frac{\rho_{l}}{2}\|\boldsymbol{x}^{l+1} - \boldsymbol{z}^{l+1} + \frac{\boldsymbol{\lambda}^{l+1}}{\rho_{l}}\|_{2}^{2} - \frac{\rho_{l}}{2}\|\frac{\boldsymbol{\lambda}^{l+1}}{\rho_{l}}\|_{2}^{2}$$

$$= \|\bar{\boldsymbol{w}} - \bar{\boldsymbol{H}}\boldsymbol{x}^{l+1}\|_{2}^{2} + \frac{\rho_{l}}{2}\|\boldsymbol{x}^{l+1} - \boldsymbol{z}^{l+1} + \frac{\boldsymbol{\lambda}^{l+1}}{\rho_{l}}\| + \frac{\rho_{l+1}}{2}\|\boldsymbol{x}^{l+1} - \boldsymbol{z}^{l+1}\|_{2}^{2}$$

$$= \|\bar{\boldsymbol{w}} - \bar{\boldsymbol{H}}\boldsymbol{x}^{l+1}\|_{2}^{2} + \boldsymbol{\lambda}^{l+1T}(\boldsymbol{x}^{l+1} - \boldsymbol{z}^{l+1}) + \frac{\rho_{l+1}}{2}\|\boldsymbol{x}^{l+1} - \boldsymbol{z}^{l+1}\|_{2}^{2}$$

$$= \|\bar{\boldsymbol{w}} - \bar{\boldsymbol{H}}\boldsymbol{x}^{l+1}\|_{2}^{2} + \boldsymbol{\lambda}^{l+1T}(\boldsymbol{x}^{l+1} - \boldsymbol{z}^{l+1}) + \frac{\rho_{l+1}}{2}\|\boldsymbol{x}^{l+1} - \boldsymbol{z}^{l+1}\|_{2}^{2}$$

$$= \|\bar{\boldsymbol{w}} - \bar{\boldsymbol{H}}\boldsymbol{x}^{l+1}\|_{2}^{2} + \boldsymbol{\lambda}^{l+1T}(\boldsymbol{x}^{l+1} - \boldsymbol{z}^{l+1}) + \frac{\rho_{l+1}}{2}\|\boldsymbol{x}^{l+1} - \boldsymbol{z}^{l+1}\|_{2}^{2}$$

$$= \|\bar{\boldsymbol{w}} - \bar{\boldsymbol{H}}\boldsymbol{x}^{l+1}\|_{2}^{2} + \boldsymbol{\mu}^{l+1}\|_{2}^{2} + \boldsymbol{\mu}^{l+1} - \boldsymbol{\mu}^{l+1}\|_{2}^{2} + \boldsymbol{\mu}^{l+1}\|_{2}^{2}$$

$$= \|\bar{\boldsymbol{w}} - \bar{\boldsymbol{H}}\boldsymbol{x}^{l+1}\|_{2}^{2} + \boldsymbol{\mu}^{l+1}\|_{2}^{2} + \boldsymbol{\mu}^{l+1}\|_{2}^{2}$$

Solving (17a) and (17b) leads to:

$$L_{\rho_l}(\boldsymbol{x}^{l+1}, \boldsymbol{z}^{l+1}, \boldsymbol{\lambda}^l) \leq L_{\rho_l}(\boldsymbol{x}^{l+1}, \boldsymbol{z}^l, \boldsymbol{\lambda}^l) \leq L_{\rho_l}(\boldsymbol{x}^l, \boldsymbol{z}^l, \boldsymbol{\lambda}^l) \quad (41)$$

Based on (17c) and (40b), (41) is converted into:

$$\|\bar{\boldsymbol{w}} - \bar{\boldsymbol{H}}\boldsymbol{x}^{l+1}\|_{2}^{2} + \frac{\rho_{l}}{2} \left\| \frac{\boldsymbol{\lambda}^{l+1}}{\rho_{l}} \right\|_{2}^{2} - \frac{\rho_{l}}{2} \left\| \frac{\boldsymbol{\lambda}^{l}}{\rho_{l}} \right\|_{2}^{2} \leq L_{\rho_{l}}(\boldsymbol{x}^{l}, \boldsymbol{z}^{l}, \boldsymbol{\lambda}^{l})$$
(42)

and

$$\|\bar{\boldsymbol{w}} - \bar{\boldsymbol{H}} \boldsymbol{x}^{l+1}\|_2^2 + \frac{\rho_l}{2} \left\| \frac{\boldsymbol{\lambda}^{l+1}}{\rho_l} \right\|_2^2 \le L_{\rho_l}(\boldsymbol{x}^l, \boldsymbol{z}^l, \boldsymbol{\lambda}^l) + \frac{\rho_l}{2} \left\| \frac{\boldsymbol{\lambda}^l}{\rho_l} \right\|_2^2.$$

From (43), we conclude that when the initial value of λ^0 is bounded, then $\|\lambda\|_2$ is bounded.

Subsequently, transforming (40c) and (40d) yields:

$$L_{\rho_{l}}(\boldsymbol{x}^{l+1}, \boldsymbol{z}^{l+1}, \boldsymbol{\lambda}^{l+1}) = \|\bar{\boldsymbol{w}} - \bar{\boldsymbol{H}}\boldsymbol{x}^{l+1}\|_{2}^{2} + (\boldsymbol{\lambda}^{l+1} - \boldsymbol{\lambda}^{l} + \boldsymbol{\lambda}^{l})^{T}(\boldsymbol{x}^{l+1} - \boldsymbol{z}^{l+1}) + \frac{\rho_{l}}{2}\|\boldsymbol{x}^{l+1} - \boldsymbol{z}^{l+1}\|_{2}^{2}$$
(44a)
$$= L_{\rho_{l}}(\boldsymbol{x}^{l+1}, \boldsymbol{z}^{l+1}, \boldsymbol{\lambda}^{l}) + (\boldsymbol{\lambda}^{l+1} - \boldsymbol{\lambda}^{l})^{T}(\boldsymbol{x}^{l+1} - \boldsymbol{z}^{l+1}) = L_{\rho_{l}}(\boldsymbol{x}^{l+1}, \boldsymbol{z}^{l+1}, \boldsymbol{\lambda}^{l}) + \rho_{l}\|\boldsymbol{x}^{l+1} - \boldsymbol{z}^{l+1}\|_{2}^{2}$$

$$L_{\rho_{l+1}}(\boldsymbol{x}^{l+1}, \boldsymbol{z}^{l+1}, \boldsymbol{\lambda}^{l+1}) = \|\bar{\boldsymbol{w}} - \bar{\boldsymbol{H}}\boldsymbol{x}^{l+1}\|_{2}^{2} + \boldsymbol{\lambda}^{l+1}^{T}(\boldsymbol{x}^{l+1} - \boldsymbol{z}^{l+1}) + \frac{\rho_{l+1} - \rho_{l} + \rho_{l}}{2}\|\boldsymbol{x}^{l+1} - \boldsymbol{z}^{l+1}\|_{2}^{2}$$

$$= L_{\rho_{l}}(\boldsymbol{x}^{l+1}, \boldsymbol{z}^{l+1}, \boldsymbol{\lambda}^{l+1}) + \frac{\rho_{l+1} - \rho_{l}}{2}\|\boldsymbol{x}^{l+1} - \boldsymbol{z}^{l+1}\|_{2}^{2}.$$

$$(44b)$$

Combining (41), (44a), and (44b), we obtain:

$$L_{\rho_{l+1}}(\boldsymbol{x}^{l+1}, \boldsymbol{z}^{l+1}, \boldsymbol{\lambda}^{l+1})$$

$$\leq L_{\rho_{l}}(\boldsymbol{x}^{l}, \boldsymbol{z}^{l}, \boldsymbol{\lambda}^{l}) + \frac{\rho_{l+1} + \rho_{l}}{2} \|\boldsymbol{x}^{l+1} - \boldsymbol{z}^{l+1}\|_{2}^{2}$$

$$= L_{\rho_{l}}(\boldsymbol{x}^{l}, \boldsymbol{z}^{l}, \boldsymbol{\lambda}^{l}) + \frac{(1+\mu)}{2\rho_{l}} \|\boldsymbol{\lambda}^{l+1} - \boldsymbol{\lambda}^{l}\|_{2}^{2}.$$
(45)

Summing (45) over l = 0, 1, ... yields:

$$L_{\rho_l}(\boldsymbol{x}^l, \boldsymbol{z}^l, \boldsymbol{\lambda}^l) \leq L_{\rho_0}(\boldsymbol{x}^0, \boldsymbol{z}^0, \boldsymbol{\lambda}^0) + \sum_{\iota=0}^{l-1} \frac{(1+\mu)}{2\rho_\iota} \|\boldsymbol{\lambda}^{\iota+1} - \boldsymbol{\lambda}^{\iota}\|_2^2.$$
(46)

Since $\|\boldsymbol{\lambda}\|_2$ is bounded, and ρ_l increases exponentially, $L_{\rho_l}(\boldsymbol{x}^l, \boldsymbol{z}^l, \boldsymbol{\lambda}^l)$ is upper bounded. Since the loss function is bounded and $\{\boldsymbol{x}^l, \boldsymbol{z}^l\}$ are variables inside it, $\{\boldsymbol{x}^l, \boldsymbol{z}^l\}$ are bounded [46]. Therefore, $\{\boldsymbol{x}^l, \boldsymbol{z}^l, \boldsymbol{\lambda}^l\}$ are bounded.

Since $\{x^l, z^l, \lambda^l\}$ are bounded sequences, the Bolzano-Weierstrass theorem [54] ensures the existence of at least one accumulation point $\{x^*, z^*, \lambda^*\}$, and we can assume that sequences $\{x^l, z^l, \lambda^l\}$ finally converge to this accumulation point. Subsequently, we derive the KKT conditions for (16), where the gradient of $L_{\rho_*}(x^*, z^*, \lambda^*)$ at x^* and the gradient of $L_{\rho_*}(x^*, z^*, \lambda^*)$ at x^* are equal to 0, given by:

$$\nabla_{\boldsymbol{x}^*} L_{\rho_*}(\boldsymbol{x}^*, \boldsymbol{z}^*, \boldsymbol{\lambda}^*)$$

$$= 2\bar{\boldsymbol{H}}^T \bar{\boldsymbol{H}} \boldsymbol{x}^* - 2\bar{\boldsymbol{H}}^T \bar{\boldsymbol{w}} + \rho_* \left(\boldsymbol{x}^* - \boldsymbol{z}^* + \frac{\boldsymbol{\lambda}^*}{\rho_*} \right) = 0$$

$$\nabla_{\boldsymbol{\lambda}^*} L_{\rho_*}(\boldsymbol{x}^*, \boldsymbol{z}^*, \boldsymbol{\lambda}^*) = \boldsymbol{x}^* - \boldsymbol{z}^* = 0.$$
(47a)

To prove the KKT condition, when $l \to 0$, the difference between \mathbf{z}^{l+1} and \mathbf{z}^{l} is:

$$\lim_{l \to \infty} \|\boldsymbol{x}^{l+1} - \boldsymbol{z}^{l}\|_{2}$$

$$= \lim_{l \to \infty} \left\| \left(2\bar{\boldsymbol{H}}^{T}\bar{\boldsymbol{H}} + \rho_{l}\boldsymbol{I} \right)^{-1} \left(2\bar{\boldsymbol{H}}^{T}\bar{\boldsymbol{w}} + \rho_{l}\boldsymbol{z}^{l} - \boldsymbol{\lambda}^{l} \right) - \boldsymbol{z}^{l} \right\|_{2}$$

$$= \lim_{l \to \infty} \left\| \left(2\bar{\boldsymbol{H}}^{T}\bar{\boldsymbol{w}} + \rho_{l}\boldsymbol{z}^{l} - \boldsymbol{\lambda}^{l} \right) / \rho_{l} - \boldsymbol{z}^{l} \right\|_{2} = 0$$
(48)

where the second and the third equations hold as $\rho_l \to \infty$ when $l \to \infty$. Therefore, when $l \to \infty$, $\lim_{l \to \infty} \|\boldsymbol{x}^{l+1} - \boldsymbol{z}^l\|_2 = 0$ and we obtain $\boldsymbol{x}^* = \boldsymbol{z}^*$. Substituting this result into (18), we

have:

$$2\bar{\boldsymbol{H}}^T\bar{\boldsymbol{H}}\boldsymbol{x}^* - 2\bar{\boldsymbol{H}}^T\bar{\boldsymbol{w}} + \boldsymbol{\lambda}^* = 0. \tag{49}$$

When $x^* = z^*$ and (49) hold, we deduce that the limit point $\{x^*, z^*, \lambda^*\}$ is a stationary point that satisfies the KKT conditions given in (47a) and (47b).

REFERENCES

- [1] F. C. M. Lau and C. K. Tse, *Chaos-Based Digital Communication Systems*. New York, NY, USA: Springer, 2003.
- [2] Y. Fang, G. Han, P. Chen, F. C. M. Lau, G. Chen, and L. Wang, "A survey on DCSK-based communication systems and their application to UWB scenarios," *IEEE Commun. Surv. Tutor.*, vol. 18, no. 3, pp. 1804–1837, Jul.-Sep. 2016.
- [3] H. Ma, G. Cai, Y. Fang, J. Wen, P. Chen, and S. Akhtar, "A new enhanced energy-detector-based FM-DCSK UWB system for tactile internet," *IEEE Trans. Ind. Informat.*, vol. 15, no. 5, pp. 3028–3039, May 2019.
- [4] G. Kaddoum and N. Tadayon, "Differential chaos shift keying: A robust modulation scheme for power-line communications," *IEEE Trans. Circuits Syst. II, Exp. Briefs*, vol. 64, no. 1, pp. 31–35, Jan. 2017.
- [5] Z. Chen, L. Zhang, J. Zhang, Z. Wu, and D. Luobu, "An OFDM-based pre-coded chaos shift keying transceiver for reliable V2V transmission," *IEEE Trans. Veh. Technol.*, vol. 71, no. 6, pp. 6710–6715, Jun. 2022.
- [6] H. Cao, Y. T. Chan, and H. C. So, "Compressive TDOA estimation: Cramér-Rao bound and incoherent processing," *IEEE Trans. Aerosp. Electron. Syst.*, vol. 56, no. 4, pp. 3326–3331, Aug. 2020.
- [7] G. Kolumbán, B. Vizvári, W. Schwarz, and A. Abel, "Differential chaos shift keying: A robust coding for chaos communication," in *International Workshop on Nonlinear Dynamics of Electronic Systems*, Seville, Spain, Jun. 1996, pp. 87–92.
- [8] H. Yang, G. P. Jiang, and J. Duan, "Phase-separated DCSK: A simple delay-component-free solution for chaotic communications," *IEEE Trans. Circuits Syst. II, Exp. Briefs*, vol. 61, no. 12, pp. 967–971, Dec. 2014
- [9] Z. Galias and G. M. Maggio, "Quadrature chaos-shift keying: Theory and performance analysis," *IEEE Trans. Circuits Syst. I, Fundam. Theory Appl.*, vol. 48, no. 12, pp. 1510–1519, Dec. 2001.
- [10] H. Yang and G. P. Jiang, "High-efficiency differential-chaos-shift-keying scheme for chaos-based noncoherent communication," *IEEE Trans. Circuits Syst. II, Exp. Briefs*, vol. 59, no. 5, pp. 312–316, May 2012.
- [11] F. Taleb, F. T. Bendimerad, and D. Roviras, "Very high efficiency differential chaos shift keying system," *IET Commun.*, vol. 10, no. 17, pp. 2300–2307, Nov. 2016.
- [12] N. Li, J.-F. Martinez-Ortega, V. H. Díaz, and J. M. M. Chaus, "A new high-efficiency multilevel frequency-modulation different chaos shift keying communication system," *IEEE Syst. J.*, vol. 12, no. 4, pp. 3334– 3345, Dec. 2018.
- [13] Z. Liu, L. Zhang, Z. Wu, and Y. Jiang, "Energy efficient parallel concatenated index modulation and M-ary PSK aided OFDM-DCSK communications with QoS consideration," *IEEE Trans. Veh. Technol.*, vol. 69, no. 9, pp. 9469–9482, Sep. 2020.
- [14] G. Kaddoum, F. D. Richardson, and F. Gagnon, "Design and analysis of a multi-carrier differential chaos shift keying communication system," *IEEE Trans. Commun.*, vol. 61, no. 8, pp. 3281–3291, Aug. 2013.
- [15] S. Li, Y. Zhao, and Z. Wu, "Design and analysis of an OFDM-based differential chaos shift keying communication system," *J. Commun.*, vol. 10, no. 3, pp. 199–205, Mar. 2015.
- [16] Z. Liu, L. Zhang, Z. Wu, and J. Bian, "A secure and robust frequency and time diversity aided OFDM-DCSK modulation system not requiring channel state information," *IEEE Trans. Commun.*, vol. 68, no. 3, pp. 1684–1697, Mar. 2020.
- [17] Y. Li, N. Seshadri, and S. Ariyavisitakul, "Channel estimation for OFDM systems with transmitter diversity in mobile wireless channels," *IEEE J. Sel. Areas Commun.*, vol. 17, no. 3, pp. 461–471, Mar. 1999.
- [18] Y. Fu et al., "BER performance of spatial modulation systems under 3-D V2V MIMO channel models," *IEEE Trans. Veh. Technol.*, vol. 65, no. 7, pp. 5725–5730, Jul. 2016.
- [19] Y. Mostofi and D. Cox, "ICI mitigation for pilot-aided OFDM mobile systems," *IEEE Trans. Wirel.*, vol. 4, no. 2, pp. 765–774, Mar. 2005.
- [20] Z. Liu, L. Zhang, and Z. Wu, "Reliable and secure pre-coding OFDM-DCSK design for practical cognitive radio systems with the carrier frequency offset," *IEEE Trans. Cogn. Commun. Netw.*, vol. 6, no. 1, pp. 189–200, Mar. 2020.

- [21] Z. Liu, H. C. So, L. Zhang, X. P. Li, and Z.-Y. Wang, "A reliable singular-vector pre-coded OFDM-DCSK system over doubly selective fading channels," *IEEE Wirel. Commun. Lett.*, vol. 13, no. 5, pp. 1453– 1457, May 2024.
- [22] R. Hadani et al., "Orthogonal time frequency space modulation," in IEEE Wireless Communications and Networking Conference (WCNC), San Francisco, CA, USA, Mar. 2017, pp. 1–6.
- [23] P. Raviteja, K. T. Phan, Y. Hong, and E. Viterbo, "Interference cancellation and iterative detection for orthogonal time frequency space modulation," *IEEE Trans. Wirel. Commun.*, vol. 17, no. 10, pp. 6501–6515, Oct. 2018.
- [24] P. Raviteja, E. Viterbo, and Y. Hong, "OTFS performance on static multipath channels," *IEEE Wirel. Commun. Lett.*, vol. 8, no. 3, pp. 745– 748. Jun. 2019.
- [25] W. Yuan et al., "New delay Doppler communication paradigm in 6G era: A survey of orthogonal time frequency space (OTFS)," China Commun., vol. 20, no. 6, pp. 1–25, Jun. 2023.
- [26] L. Gaudio, G. Colavolpe, and G. Caire, "OTFS vs. OFDM in the presence of sparsity: A fair comparison," *IEEE Trans. Wirel. Commun.*, vol. 21, no. 6, pp. 4410–4423, Jun. 2022.
- [27] Z. Zhou, L. Liu, J. Xu, and R. Calderbank, "Learning to equalize OTFS," IEEE Trans. Wirel. Commun., vol. 21, no. 9, pp. 7723–7736, Sep. 2022.
- [28] M. Mohammadi, H. Q. Ngo, and M. Matthaiou, "Cell-free massive MIMO meets OTFS modulation," *IEEE Trans. Commun.*, vol. 70, no. 11, pp. 7728–7747, Nov. 2022.
- [29] A. S. Bora, K. T. Phan, and Y. Hong, "Mitigating spatial correlation in MIMO-OTFS," *IEEE Trans. Veh. Technol.*, vol. 73, no. 3, pp. 3608– 3622, Mar. 2024.
- [30] Z. Sui, H. Zhang, S. Sun, L.-L. Yang, and L. Hanzo, "Space-time shift keying aided OTFS modulation for orthogonal multiple access," *IEEE Trans. Commun.*, vol. 71, no. 12, pp. 7393–7408, Dec. 2023.
- [31] Z. Sui, H. Zhang, Y. Xin, T. Bao, L.-L. Yang, and L. Hanzo, "Low complexity detection of spatial modulation aided OTFS in doubly-selective channels," *IEEE Trans. Veh. Technol.*, vol. 72, no. 10, pp. 13746–13751, Oct. 2023.
- [32] M. Isik, M. Nkomo, A. Das, and K. R. Dandekar, "FPGA implementation of OTFS modulation for 6G communication systems," in 2023 IEEE Future Networks World Forum, Baltimore, MD, USA, Nov. 2023, pp. 1–7.
- [33] L. Xiang, Y. Liu, L.-L. Yang, and L. Hanzo, "Gaussian approximate message passing detection of orthogonal time frequency space modulation," *IEEE Trans. Veh. Technol.*, vol. 70, no. 10, pp. 10999–11004, Oct. 2021.
- [34] J. A. Zhang, H. Zhang, K. Wu, X. Huang, J. Yuan, and Y. J. Guo, "Wireless communications in doubly selective channels with domain adaptivity," *IEEE Commun. Mag.*, vol. 63, no. 5, pp. 102–108, May 2025
- [35] K. R. Murali and A. Chockalingam, "On OTFS modulation for high-Doppler fading channels," in *Information Theory and Applications* Workshop (ITA), San Diego, CA, USA, Feb. 2018, pp. 1–10.
- [36] T. Thaj and E. Viterbo, "Low complexity iterative rake decision feedback equalizer for zero-padded OTFS systems," *IEEE Trans. Veh. Technol.*, vol. 69, no. 12, pp. 15606–15622, Dec. 2020.
- [37] Q. He, P. Ding, P. Chen, Y. Fang, and Z. Lin, "Doppler resilient orthogonal time-frequency space (OTFS) systems based on differential chaos shift keying," in *IEEE/CIC International Conference on Commu*nications in China (ICCC Workshops), Dalian, China, Aug. 2023, pp. 1–6.
- [38] J. Zheng, L. Zhang, Y. Li, Y. Ouyang, and H. Zhuang, "An orthogonal time frequency space modulation based differential chaos shift keying transceiver for reliable communications," in *IEEE 97th Vehicular Tech*nology Conference (VTC2023-Spring), Florence, Italy, Jun. 2023, pp. 1–5.
- [39] Z. Liu, H. C. So, L. Zhang, and X. P. Li, "Robust receiver for OFDM-DCSK modulation via rank-1 modeling and ℓ_p -minimization," *Signal Process.*, vol. 188, p. 108219, Nov. 2021.
- [40] L. Zhang, J. Zheng, B. Chen, and Z. Wu, "Reliable low-rank approximation of matrices detection aided multicarrier DCSK receiver design," *IEEE Syst. J.*, vol. 15, no. 4, pp. 5277–5288, Dec. 2021.
- [41] Z. Liu, H. C. So, X. P. Li, L. Zhang, and Z.-Y. Wang, "Robust and energy efficient sparse-coded OFDM-DCSK system via matrix recovery," *IEEE Trans. Commun.*, vol. 71, no. 8, pp. 4839–4850, Aug. 2023.
- [42] C. C. Paige and M. A. Saunders, "LSQR: An algorithm for sparse linear equations and sparse least squares," ACM Trans. Math. Softw., vol. 8, no. 1, pp. 43–71, Mar. 1982.

- [43] B. Van Nguyen, M. Le, H. Jung, and K. Kim, "Antijamming receiver with hybrid blanking-clipping for DCSK system," *IEEE Trans. Aerosp. Electron. Syst.*, vol. 56, no. 5, pp. 3751–3761, Oct. 2020.
- [44] P. Raviteja, Y. Hong, E. Viterbo, and E. Biglieri, "Practical pulse-shaping waveforms for reduced-cyclic-prefix OTFS," *IEEE Trans. Veh. Technol.*, vol. 68, no. 1, pp. 957–961, Jan. 2019.
- [45] G. D. Surabhi, R. M. Augustine, and A. Chockalingam, "On the diversity of uncoded OTFS modulation in doubly-dispersive channels," *IEEE Trans. Wirel. Commun.*, vol. 18, no. 6, pp. 3049–3063, Jun. 2019.
- [46] Z.-Y. Wang, H. C. So, and A. M. Zoubir, "Low-rank tensor completion via novel sparsity-inducing regularizers," *IEEE Trans. Signal Process.*, vol. 72, pp. 3519–3534, Jun. 2024.
- [47] W. C. Jakes and D. C. Cox, Microwave Mobile Communications. Hoboken, NJ, USA: Wiley-IEEE Press, 1994.
- [48] A. Goldsmith, Wireless Communications. Cambridge, UK: Cambridge University Press, 2005.
- [49] M. Barkat, Signal Detection and Estimation, ser. Artech House Radar Library. Boston, MA, USA: Artech House, 2005.
- [50] E. Biglieri, P. Raviteja, and Y. Hong, "Error performance of orthogonal time frequency space (OTFS) modulation," in 2019 IEEE International Conference on Communications Workshops, Shanghai, China, May 2019, pp. 1–6.
- [51] G. Cheng, L. Wang, W. Xu, and G. Chen, "Carrier index differential chaos shift keying modulation," *IEEE Trans. Circuits Syst. II Express Briefs*, vol. 64, no. 8, pp. 907–911, Aug. 2017.
- [52] Z. Liu, L. Zhang, Z. Wu, and J. Bian, "Carrier interferometry code index modulation aided OFDM-based DCSK communications," in *IEEE 90th Vehicular Technology Conference (VTC2019-Fall)*, Honolulu, HI, USA, Sep. 2019, pp. 1–5.
- [53] T. Xie, Z. Lu, Q. Han, J. Quan, and B. Wang, "Low-complexity LSQR-based linear precoding for massive MIMO systems," in *IEEE 82nd Vehicular Technology Conference (VTC2015-Fall)*, Boston, MA, USA, Sep. 2015, pp. 1–5.
- [54] R. G. Bartle and D. R. Sherbert, *Introduction to Real Analysis*, 4th ed. Hoboken, NJ, USA: Wiley, 2011.